ABSTRACT

Title of Thesis: 3D IMAGE ANALYSIS OF CT DATA OF CONCRETE CYLINDERS UNDERGOING DELAYED ETTRINGTIE FORMATION
Kuo Shi
Master of Science, 2019

Thesis Directed By: Professor Amde M. Amde, Civil and Environmental Engineering & Professor Richard Livingston, Materials Science and Engineering

The strains in a concrete caused by delayed ettringite formation (DEF) are conventionally expressed in terms of the one-dimensional linear expansion. However, concrete is not a homogeneous material, and differences in the volume change between the inert aggregates and the reactive cement paste will produce variations in local displacements that cannot be detected by the linear expansion variable. With CT slices offered by Simultaneous neutron and X-ray computed tomography (SNXCT), this thesis applies image analysis algorithms to quantify the distortion of cylinder over time due to delayed ettringite formation. The research reported in this thesis concerned the development of several MATLAB programs to apply image analysis algorithms to quantify the distortion of cylinder over time in terms of summary variables. These included mean radial expansion, deviation from circularity, vertical tilt angle and rotation, void area fraction and the displacement of microbead internal reference points.

3D IMAGE ANALYSIS OF CT DATA OF CONCRETE CYLINDERS
UNDERGOING DELAYED ETTRINGITE FORMATION

by

Kuo Shi

Thesis submitted to the Faculty of the Graduate School of the
University of Maryland, College Park, in partial fulfillment
of the requirements for the degree of
Master of Science
2019

Advisory Committee:
Professor Dr. Amde M. Amde, Chair
Professor Mohamad I. Al-Sheikhly
Professor Mohamed Sherif Aggour

Acknowledgement

I really want to thank Professor Amde M. Amde and Professor Richard Livingston for their support and guiding me through all the research and writing process. Their remarkable patience and rigorous attitude really get me impressed and benefits me.

I also want to thank my colleague Dr. Serge Alain Feuze Lekem for his collaboration and enthusiastic support.

Table of Contents

List of Tables

List of Figures

Chapter 1. Introduction

■ *<u>Background Information</u>*

The durability of concrete has been always a hot research topic. Premature

deterioration of concrete materials is one of the main causes of structural failure and it

also results expenditures for repair and replacements. Delayed ettringite formation

(DEF), as an aggressive substance generated internally, is one of the reasons causing

premature deterioration. In 1965, R. A. Kennerley (1965) was the first who studied

delayed ettringite formation might be an issue causing the destruction of concrete

since then the research of DEF has been paid attention to by many scholars.

DEF can be defined as the formation of ettringite after the cement paste, mortar or

concrete has completely hardened with no exposure to external sulfate ion. (Taylor et

al. 2001) SO_3 and Al_2O_3 are the main components of ettringite, so it is said that the

content and proportion of both in cement will affect the expansion of DEF. In standard

curing conditions, the first formation of ettringite in Portland cement is the result of

the reaction of tricalcium aluminate with sulfate ions in the pore solution. After the

phase of concrete hardening, the second formation of ettringite appears which is the

main cause of potential damage and ultimately leads to the destruction of concrete.

Ghorab et al.'s (1980) research and many other studies indicate that there are two

necessary conditions for expansion due to DEF. First, the material should have been

through a certain period time in an environment of not less than 70°C. Then, after

returning to normal temperature, the material needs to be placed in a relatively humid environment. If the above two conditions are satisfied, the expansion caused by DEF will occur. In addition, from the research of Yang et al. (1999), 40x40x1600-mm mortar prism is cured at 100°C and kept in water, it turns out that the obvious expansion will generally appear in a few months and will be completed in the next one to two years.

The mechanism of the expansion of DEF has become a heated topic of debate since DEF was identified. Several researches and studies concentrated on how the expansion of DEF has an effect on concrete and inflict damage on the structure of concrete, however, there is still no agreement on the expansion mechanism associated with DEF. At present, there are mainly three theories of expansion mechanism. First is the swelling theory of expansion proposed by Mehta in 1973. This hypothesis proposed by Mehta illustrates that the ettringite is a sort of colloidal, expansive particle. The water can be absorbed by these particles and the expansion occurs consequently. The second one is theory of crystal growth proposed by Fu et al. (1996), Scherer (1999), and Taylor et al. (2001) At high temperature, due to the adsorption of the C-S-H gel, the C-S-H gel can adsorb sulfate at first and then slow desorption of sulfate which are essential for the formation of delayed ettringite formation. The third theory suggested by Taylor is uniform paste theory. It indicates that the ettringite replaces the monosulfate distributing in the paste uniformly and recrystallizes in the cracks of the paste and aggregate interfaces. These three theories are the most

concerned theories within the scientific community. In order to further study the expansion mechanism of DEF, this paper needs to explore the distortion of concrete samples.

- ### *Problems Statement and Approaches*

The existence of delayed ettringite formation in concrete can reduce the stiffness and strength of concrete, which is a factor altering the durability of concrete. Although many scholars and researchers have spent a lot of time and resources to study it, there is still no widely accepted version on the expansion mechanism of DEF. To better understand the expansion mechanism of DEF, an investigation of it was performed using the nondestructive analytical method of simultaneous neutron and X-ray computed tomography (SNXCT) along with conventional test methods (Feuze 2019). Three concrete specimens were cast with varying conditions specific treatments to generate to promote or inhibit DEF. They were scanned by SNXCT seven times over a period of 300 days. This produced a collection of data containing reconstruction 3-D images of the interior of the specimens at a resolution of 25 µm.

This thesis takes advantage of the availability of these data sets to investigate the application of several image analysis algorithms to quantify the changes in the shape of a concrete object undergoing expansive stress. DEF damage is conventionally quantified in terms of the one-dimensional linear expansion variable measured by ASTM C157.The assumption has been that it could be applied to a 3-dimensional volume which implies that the expansion is the same in all three directions, i.e.,

uniform volumetric expansion.   However, concrete is not a homogeneous material and the differences in the volume change between the internal aggregates and the cement paste will produce variations in local displacements that are more likely to produce non-uniform expansion. The anticipated outcome of this research would be a set of macroscopic statistics of the DEF process that would more fully and accurately describe the deformations and thus lead to a better understanding of the mechanisms and kinetics involved. The ability to obtain these deformation statistics from the object itself would make the C157 linear measurement redundant and thus eliminate the need to cast a separate set of concrete prisms and to make labor-intensive measurements on them.

The research approach had several objectives:

- Quantify uniform volumetric component by the change in mean radius

- Quantify deviatoric component by distortion from circularity by Fourier series analysis of radial distortion

- Quantify internal distortion by displacements of the centroid (tilt angle) and embedded reference points (microbeads)

- Quantify ettringite growth in voids by the void area ratio

Chapter 2. Previous Laboratory Work

In order to be able to understand the results of applying the image analysis algorithms to SNXCT data sets, it is necessary first to review the work of Feuze et al. in acquiring them.

- *Sample Preparation*

In this research, the concrete samples were prepared at the National Ready Mix Concrete Association Laboratory (NRMCA) in greenbelt, Maryland and the Civil Engineering Lab of the University of Maryland at College Park. ASTM C192-16, Standard Practice for Making and Curing Test Specimens in the Laboratory, was followed to prepare the concrete samples. In previous work, it was found that potassium added to concrete can accelerate the rate of DEF (Ceesay 2007).

Three types of concrete specimens were prepared. These are summarized in Table 1. The control set, DP1-3, had normal level of potassium (0.79% K_2O by weight of cement) The other two were heat-treated to induce micro-cracks. Set DP1-2 was also made with high potassium content (1.72% K_2O by weight) to promote DEF. The fourth possibility was not used because previous has shown that without micro-cracks DEF takes too long to develop.

Table 1: Potassium Level for Concrete Specimens

	Potassium level	
	Normal	High
	0.79% K_2O	1.72% K_2O

| Heat treatment | No | DP1-3 | N/A |
| | Yes | DP1-1 | DP1-2 |

For each type, three different shapes of specimens were cast including 3in. x 3in. x
11.25in. prisms, 4in. x 8in. concrete cylinders and 2in. x 2in. concrete cylinders. The
specimens in three different sizes have different experimental purposes. 3in. x 3in. x
11.25in. prisms are for measurement of weight change and measurement of
expansion. 4in. x 8in. concrete cylinders are used for testing the compressive strength
of the concrete specimens. 2in. x 2in. concrete cylinders are used in the SNXCT
analysis.

The three types of microbeads inserted in the 2in. x 2in. concrete cylinders were
stainless steel, barium titanite and polystyrene. The selection of the constituent
material of microbead is according to the attenuation factors and applicability. With
the existence of these beads, the grayscale of the image can be calibrated to help the
image segmentation process (Feuze 2019). In the specimen with 2in. x 2in.
dimension, the microbeads are placed at different locations during casting.

Table 2: Distribution of Microsphere Standards in Concrete Cylinders

Layer Height (in)	Number of microspheres			Material	Diameter mm
	DP1-1	DP1-2	DP1-3		
0.5	5	5	~5	polystyrene	1.95
1.0	5	5	6	barium titanate	0.85
1.5	8	~9	9	stainless steel	0.88

*Heights are inverted for this specimen
** Partial slumping during handling

The sample microbeads placed as shown in the figure below.

Figure 1. Placement of microbeads (Feuze 2019)

The heat treatment consisted of 3 cycles was applied about 48 hours after casting (Amde and Livingston 2013). The high temperature during the heat treatment was 82° C and the relative humidity kept at 100%.

- *SNXCT scans*

Neutron imaging and X-ray tomography both belong to the two methods of radiographic testing branch in nondestructive testing. Through SNXCT, the damage caused by DEF in concrete, the distortion and inclination of specimen can be quantified through subsequent data processing. The scanning was done at the Neutron and X-ray CT (NeXT) system of the Neutron Research Center (NCNR) at the National Institute of Standards and Technology (NIST) in Gaithersburg, Maryland. The three concrete cylinder specimens with 2in. x 2in. dimension were scanned at 9 days, 66 days, 102 days, 148 days and 230 days after casting. The scan dates are indicated in Figure 2, which is a plot of the linear expansion data versus time. The quality of the results of the first three tomography tests was very poor so the images

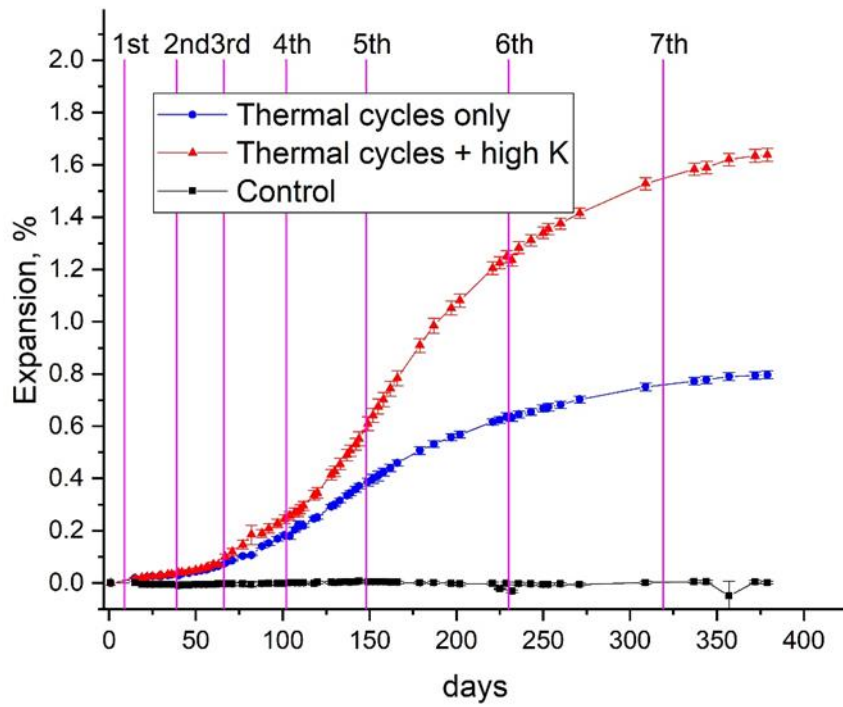of the first three trials were not used in this study.

Figure 2: Linear expansion of specimens versus time

Chapter 3. Radial Distortion Analysis

After the previous preparation work completed, the concrete samples which are suitable for this study have been finished. To understand the expansion mechanism of DEF in the samples, an appropriate model that can represent the radial distortion of the samples becomes a key point. The question is how to convert these images of tomography into a 3-dimensional model that is available to perform the volume of the sample. A Virtual Reality Modeling Language technique may be an answer to this question since it can deliver a definite 3-D view of a certain object. Erdogan (Erdogan et al. 2006) proposed a method to obtain the visual reality model of aggregate particles. Erdogan developed an effective process to collect the shape data of aggregate particle and accomplish a 3-D particle reconstruction from 2-D slices. A mathematical model that could predict the possible effects of particles on concrete performance was generated through the virtual reality modeling language and spherical harmonic series, combining with the data of actual particle shape. The particle shape can be described by the spherical harmonic mathematical analysis, a transformation of spherical harmonic function. However, characterizing the shape of a cylinder mathematically is different from the shape of the particle. Based on my understanding, the harmonic function is not able to be effectively utilized or transformed in this case. Considering it is challenging to make 3-dimensional reconstruction model directly, it is simpler to start with 2-dimensional model as another clue and stack the slices to derive the 3-dimensional model. In order to

achieve that, the slice is depicted by MATLAB software. Each slice is performing the image of cross-section of the concrete cylinder.

Before cutting into the topic, preliminary work is applied to raw slice as an example shown in Figure 3 (a). To avoid potential interference, objects containing fewer than 30 pixels, which probably are caused by low resolution of tomography, are removed from the image and then enclose the target area to get a clear shape. Transform the image into grayscale and all the boundary points on the circle can be identified according to the matrix of grayscale value. Find the center of mass of the shape. After that, the surface coordinates of the object are found in digital form at a given angle by extending the straight segment from the centroid to the point just passing through the digital surface of the object. The length of line segment and the angle can be recorded.
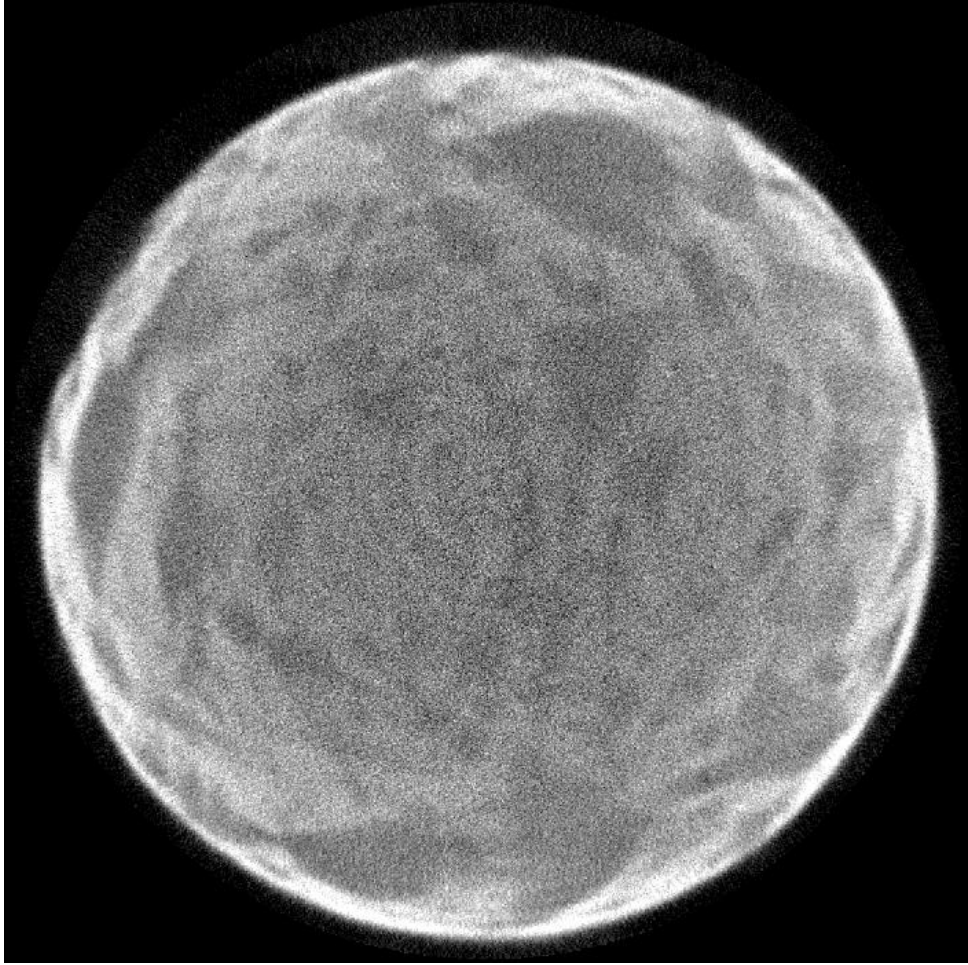
(a)
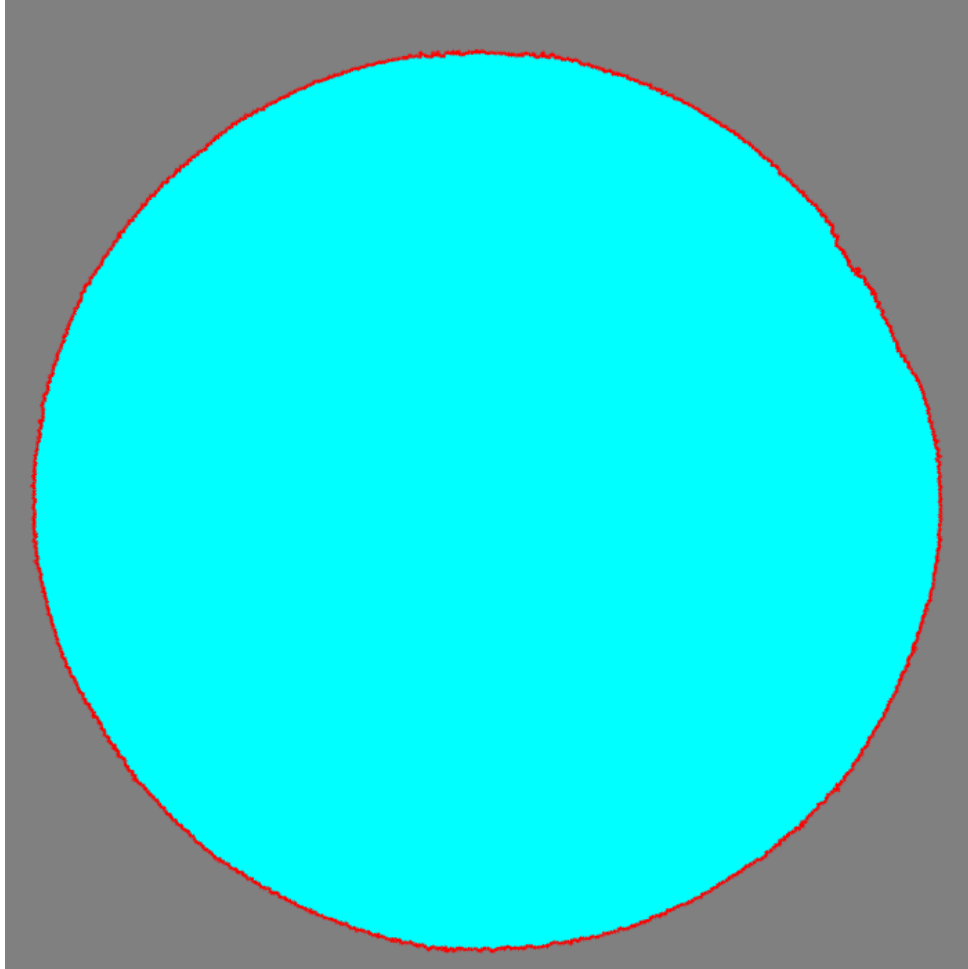
(b)

Figure 3. (a) is the original image; (b) is the image after processing

Creating a 2-D model essentially means finding a mathematical function that can summarize the laws of the graph based on these boundary points. E.J. Garboczi (2002) proposed that Gaussian quadrature and Fourier analysis can be utilized to derive the 2-D model. Garboczi used Gaussian quadrature for doing integrals numerically and exploited Fourier analysis to finally get the equation:

$$R(\theta) \approx \sum_{j=0}^{N} [a_j \cos(j\theta) + b_j \sin(j\theta)]$$

Where the value of a_j and b_j comes from integrals:

$$a_j = \frac{1}{2\pi} \int_0^{2\pi} R(\theta) \cos(j\theta)\, d\theta$$

$$b_j = \frac{1}{2\pi} \int_0^{2\pi} R(\theta) \sin(j\theta)\, d\theta$$

Where

$R(\theta)$ is the distance between the center of mass and the surface at angle θ

θ, from 0 to 2π, is the angle measured counterclockwise from x-axis to the arbitrary

point on the surface

j is the Fourier coefficient

Through calculation by MATLAB, plot all points in R and derive the reconstructed

image. The computed target image is derived as shown in Figure 4. When j value

equals one, the shape is almost a perfect circle. The shape of the object gradually

changes as the value of j increases.

(a)

14
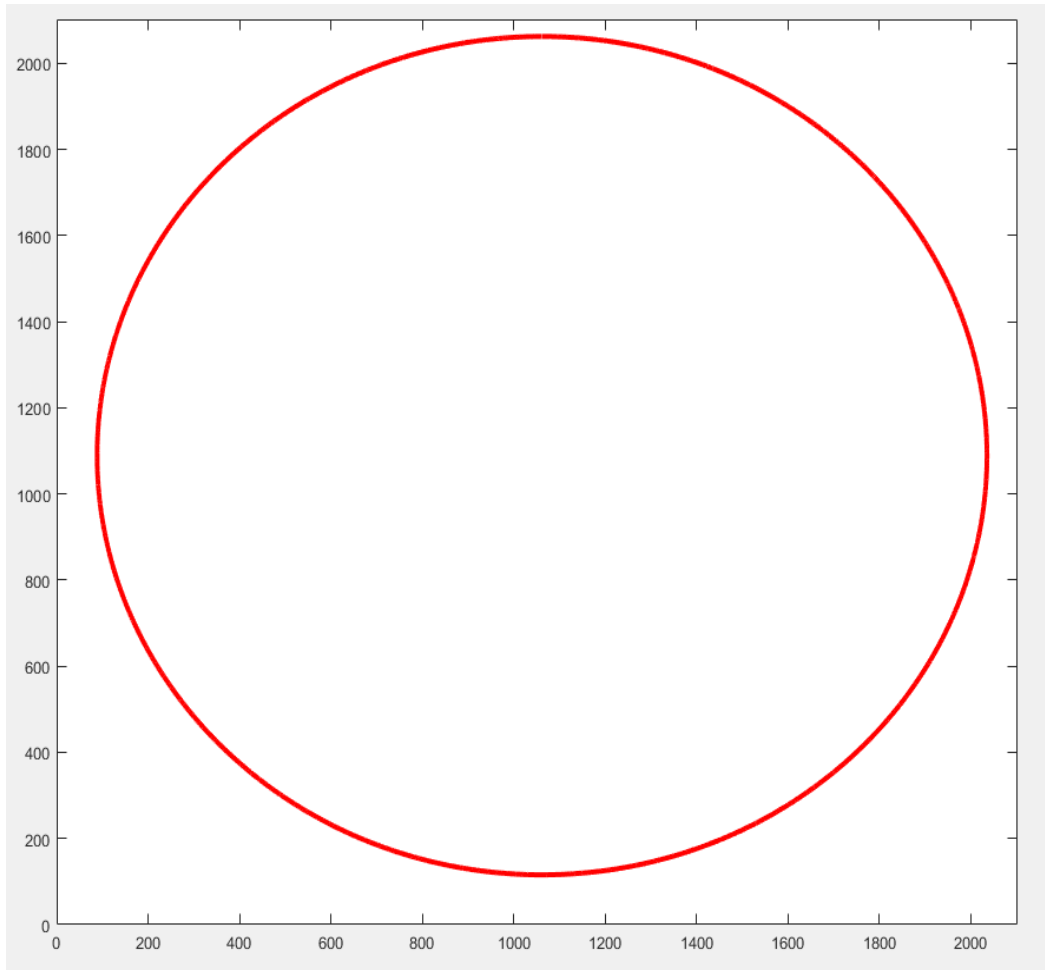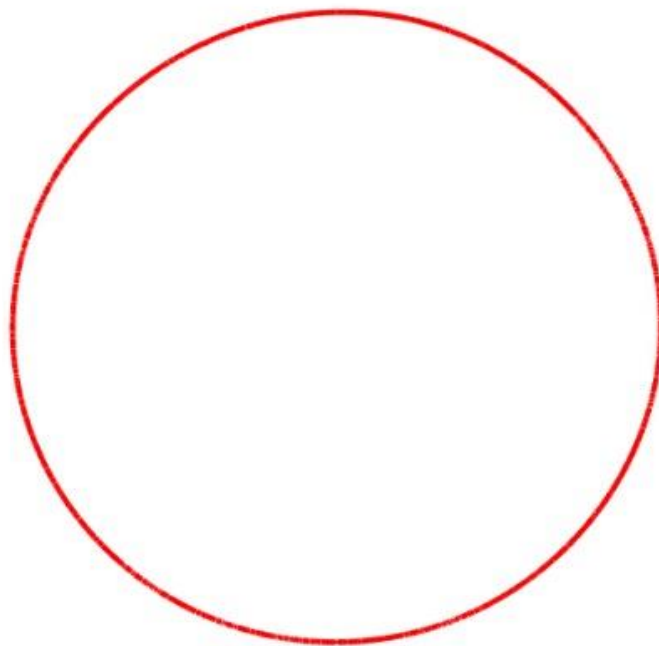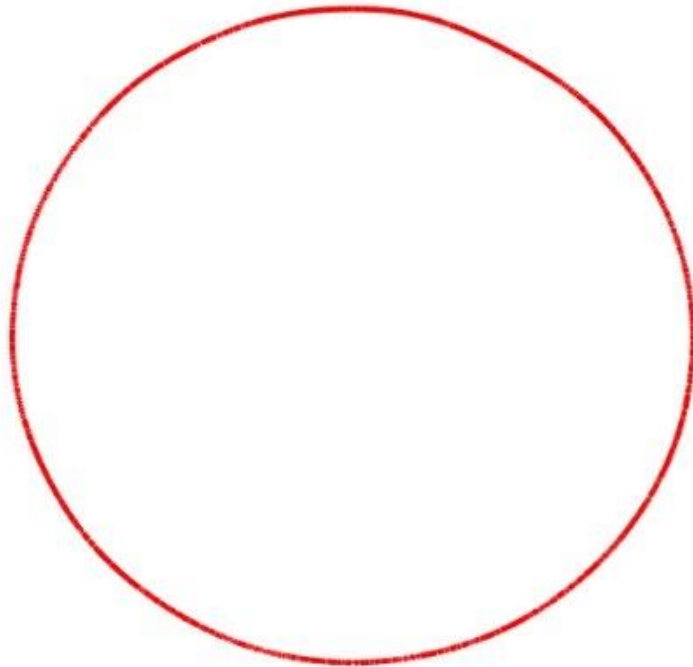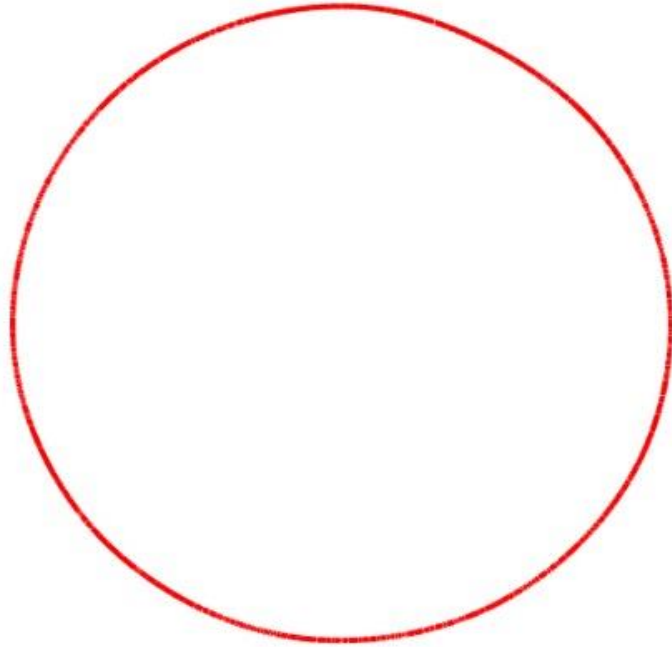
(b)
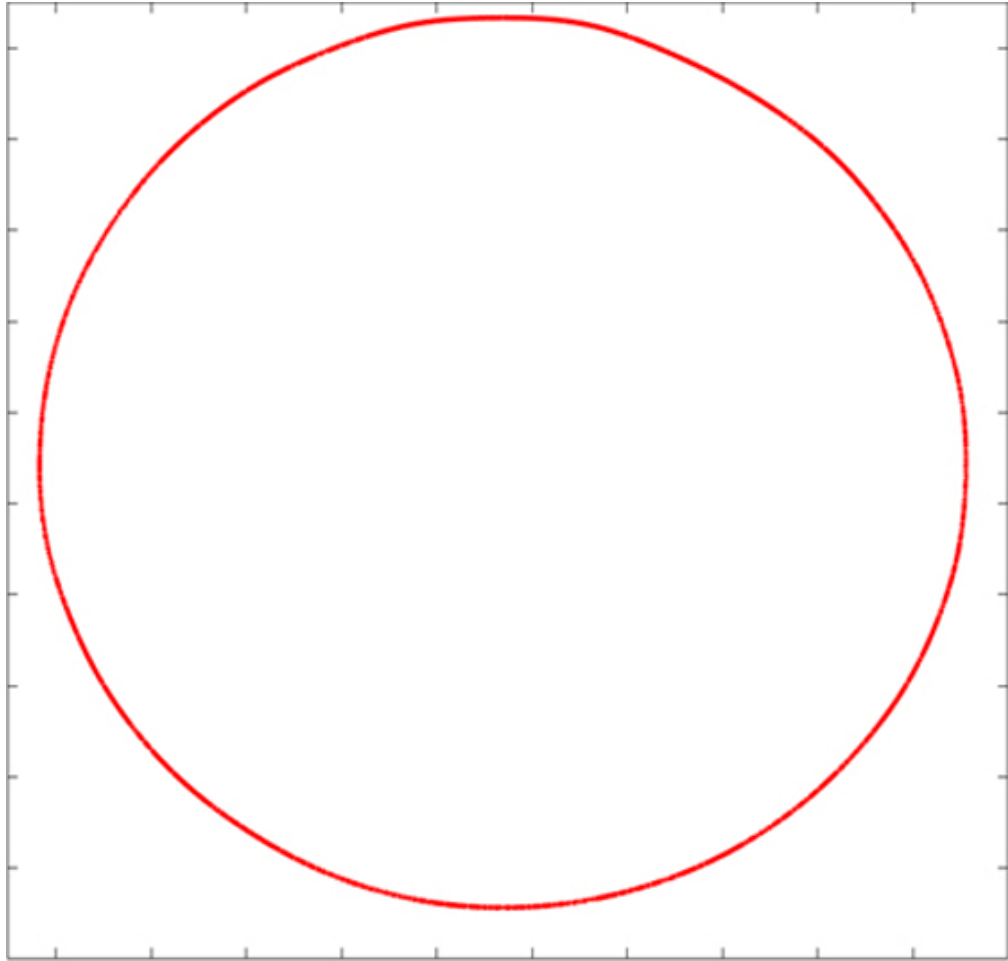
(c)

Figure 4: (a) when j=1; (b) represents j=5, j=10, j=15, from top to bottom, respectively; (c) when j=20

　　Even though the deformation of the shape is subtle, in Figure 4 (b), it is still

visually detectable. The gradual change of shape can be observed in Figure 4 (b).

Comparing with the real shape shown in Figure 3 (b), the curvature of the arc on the

upper right corner of the circle in Figure 4 (b) becomes smaller and the computed

shape is matching the real shape to some extent. As the j value increases, it is can be

seen that the computed shape has a trend to fitting the real shape.
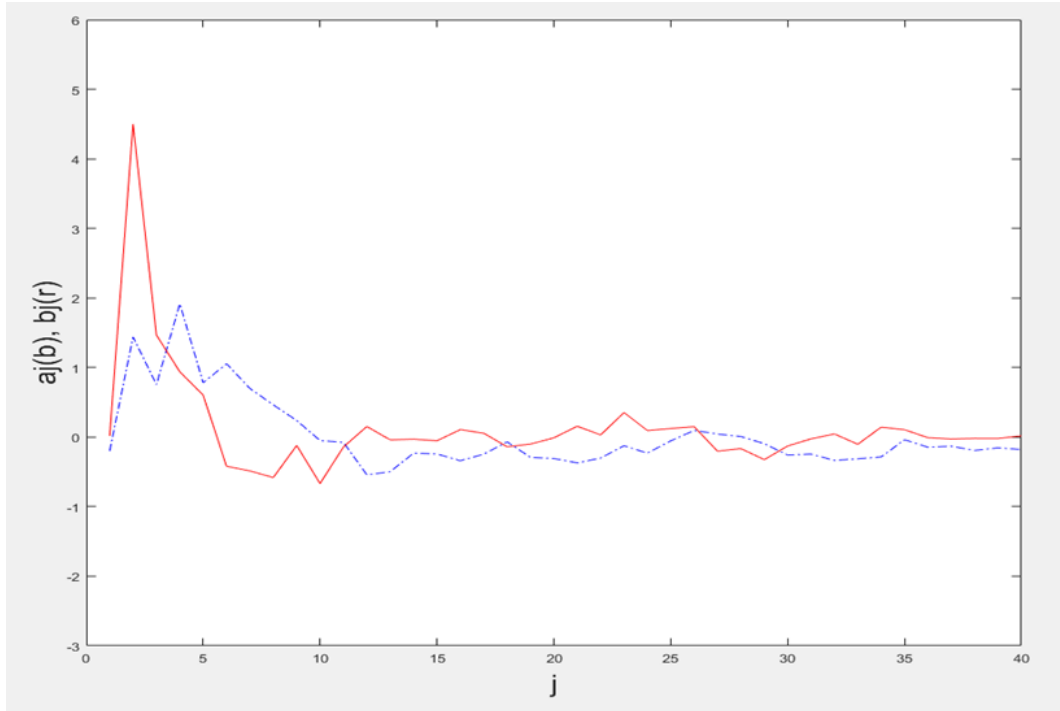
Figure 5:The value of a_j and b_j vs. j. Red line represents a_j. Blue dash line represents b_j

Note that the shape of the plot of $a_j\ and\ b_j$ vs. value of j in Figure 5. also shows

consistency of this feature. The value of $a_j\ and\ b_j$ has fluctuation in early phases

and it becomes smaller and smaller as the value of j increases. By j= 15, the

fluctuation nearly get eliminated as a result of negligible values of coefficient

$a_j\ and\ b_j$. When the value of j reaches a certain point, the shape created under higher

order values of j has a trend of fitting the digital structure of the exterior of the object

pixel-to-pixel. (Garboczi, 2002) Although some evidence is collected to prove that

this method is effective for this shape, it is still not convincing enough to draw this

conclusion. Computing the area of the result is a reliable way to clearly show the

practicality of this method.

17
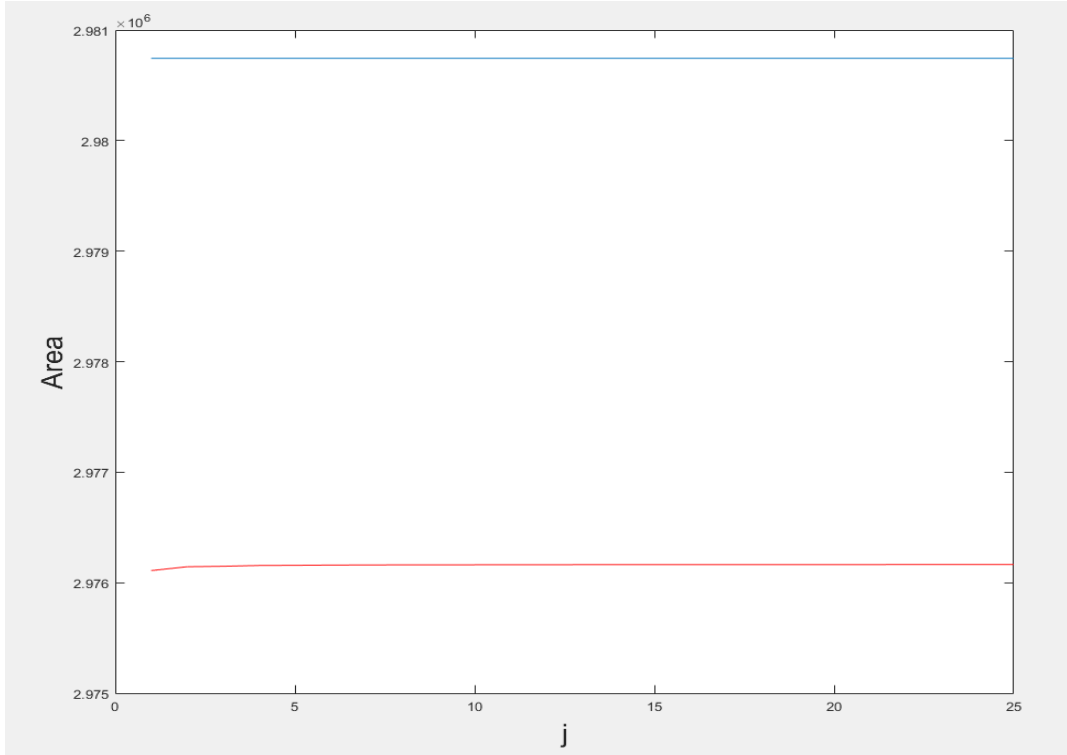
Figure 6:Area comparison of computed area (red) and digital area (blue)

The area A of computed shape is calculated through equation (Garboczi 2002):

$$A = \frac{1}{2} \int_0^{2\pi} [R(\theta)]^2 d\theta = \pi a_0^2 + \frac{\pi}{2} \sum_{j=1}^{N} (a_j^2 + b_j^2)$$

Figure 6 shows the result of comparing the digital area and computed area, the computed area is represented by the red line and the blue line represents the original digital area. In ideal status, the computed area should have a tendency to fit the digital area as the value of j becomes larger, but there is only a clear transition in the first three phases. After j=3, the changing value of computed area is almost negligible. The error between the computed area and real area is around 0.15% even if the value of j is raised to 100. Since the number of reference points on the surface of the circle is finite, the result will always be slightly inaccurate and that may be an explanation of the inevitable error for this case. In addition, from created shape, the roughness is not

18

distinct while observing by naked eyes.

Knowing the defect of expressing the roughness, calculating the mean radius of each slice can also provide some valuable information. The shape is formed by all reconstructed points on the boundary so the distances between the centroid and these points are considered as radius. Calculate the mean radius for each slice and collect all results of an entire cylinder. Once the mean radius of a cylinder can be drawn, the variance of the radius will get calculated. The variance can show how the radius of the slices deviates from the average radius. If the linear expansion in concrete cylinder occurs, the variance could be a key point in comparing the linear expansion of different concrete specimens. The hypothesis is that a larger variance indicates a larger linear expansion in concrete specimen. The result of variance analysis is shown in Table 3.

Table 3: Variance analysis of radius of cylinder

Serial Number	Mean Radius (pixels)	Variance
DP1-1-4	952.3122	30.58984
DP1-1-5	958.8883	23.21969
DP1-1-6	964.8519	16.37402
DP1-2-4	929.459	13.37348
DP1-2-5	941.8385	17.70317
DP1-2-6	925.6802	3.921649
DP1-3-4	943.6265	2.574867

DP1-3-5	926.434	1.234994
DP1-3-6	931.5896	3.354573

The variance and the mean radius listed here are adjusted based on the size of the image. Each time of tomography provides different sizes of image. The results in Table 3 have all been rescaled.

The smallest variance is for the control specimens. The square root of the variance is the standard deviation which is the uncertainty of the radius measurement. For the control specimens, the average of the three mean radius is 934 pixels and the standard deviation is about 1.5 pixels. This implies that the minimum radial strain that could be detected would be 0.1%. This is the same order of magnitude as the observed linear expansion. However, the variance of the mean radius with height increased by an order of magnitude going from the control specimen to the heat-treated one, which indicates non-uniform volumetric expansion. This also suggests that the variance could be a useful statistic.

Chapter 4. Tilt Analysis

- *Tilt Angle of Specimens*

This section discusses the tilt analysis of the concrete specimens using the images

from tomography. The method using Gaussian quadrature and Fourier analysis to

create a 2-dimensional model is not meeting the expectation, therefore, an efficient

method is required so that the distortion analysis of cylindrical concrete samples could

continue. With existing equipment conditions and knowledge, it is arduous to directly

build a visual model that can represent the entire cylinder. Studying the distortion of

cylindrical samples from the side may be a more practical idea. Tilt analysis including

determining tilt angle of cylinder and horizontal rotation angle of the axis of the

cylinder is considered as a complementary method. Through tilt analysis, the results

may not be as intuitive as building a 3-dimensional model, but it will also be a great

help to the research. Determining the tilt angle and the distortion of the cylinder are

both achieved by measuring the center of the slice whose shape is an approximate

circle. C. J. Sangwin (2006) proposed that the center of mass of an equal density

cylinder is on the axis of the cylinder. Although the real density of the cylinder is not

uniform, the line connected by the centroid of slices can be regarded the axis of the

cylinder. The coordinate of center of mass in slice is calculated using equation:

$$\overrightarrow{X_M} = \frac{\sum_i x_i}{\sum_i 1}$$
$$\overrightarrow{Y_M} = \frac{\sum_i y_i}{\sum_i 1}$$

With the equation above, process all images of one specimen using MATLAB to

calculate the centroid of every single slice. The software counts all pixels inside the

boundary of the shape and calculates the center of mass of the area composed by

counted pixels. To avoid affecting the process of calculating centroid due to residual

regions outside target shape, use MATLAB remove all objects smaller than 500

pixels. Repeat the steps for all specimens and their tomography results so preliminary

work of acquiring data is finished. After processing all slices, connect all centroids

and perform the line in 3-dimensional space. The sample figure is shown below:
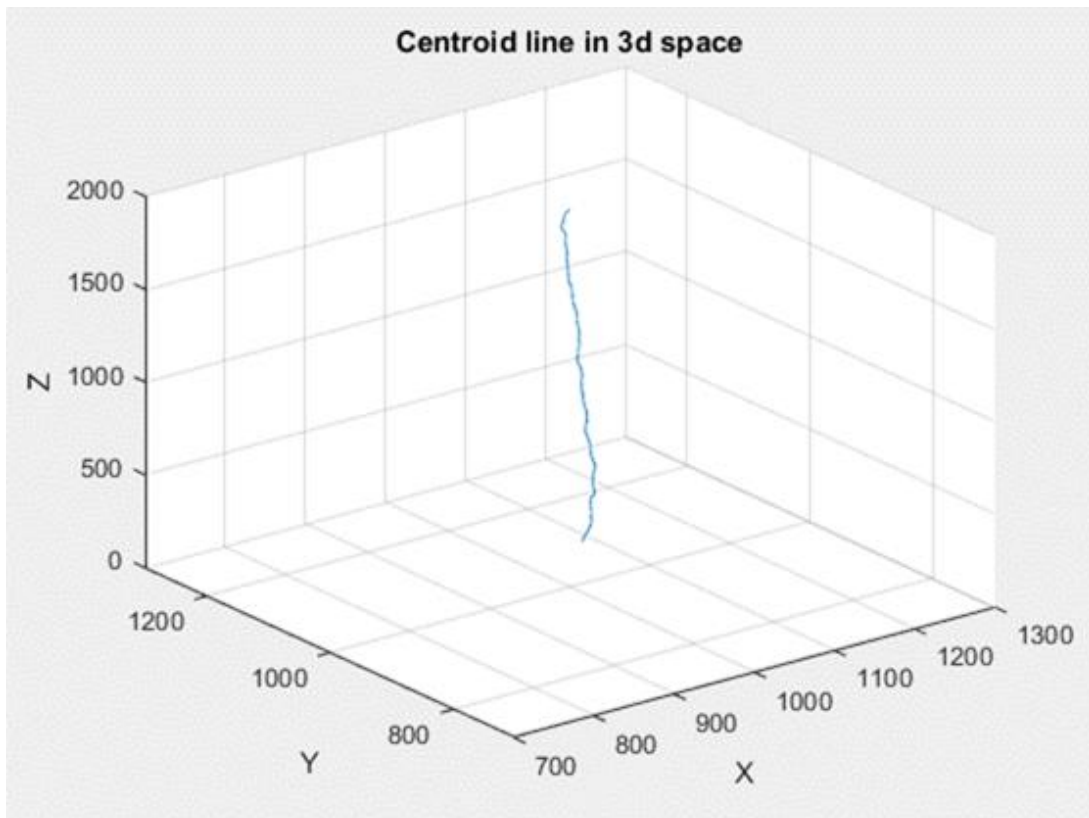

Figure 7: Centroid line drawing of trial DP1-2-6. DP1-2-6 represents the result of sixth
tomography of set 2

　　The data resource of Figure 7. is from the result of sixth tomography on set 2

(with added potassium). The unit of x axis and y axis is pixel. Z axis represents the

height of the cylinder. From the figure, the tilt of axis of the concrete cylinder can be

intuitively exhibited. To quantify the tilt of the axis, more procedures are required.

There is also an alternative way to determine the center by locating the midpoints of two lines. First line connects two boundary points that have maximum and minimum value in horizontal direction and second line connects two points on the boundary having maximum and minimum value in vertical direction. Take the x value of midpoint of the first line and y value of midpoint of the second line as center. Using this method, the result is not consistent with the result using the method mentioned above. The differences of coordinates of centroids between two methods are not negligible. Considering the roughness of the shape and residual parts outside the shape, even if the method can possibly export right answer, the result from this method will be nether accurate nor convincing. In general, a better way is to use the center of mass as the centroid of the shape.

The tilt analysis is an essential outcome reaped from the data of centroid. It is mainly about getting the tilt angle between the line of centroids and perpendicular axis. The angle θ is shown in Figure 8.
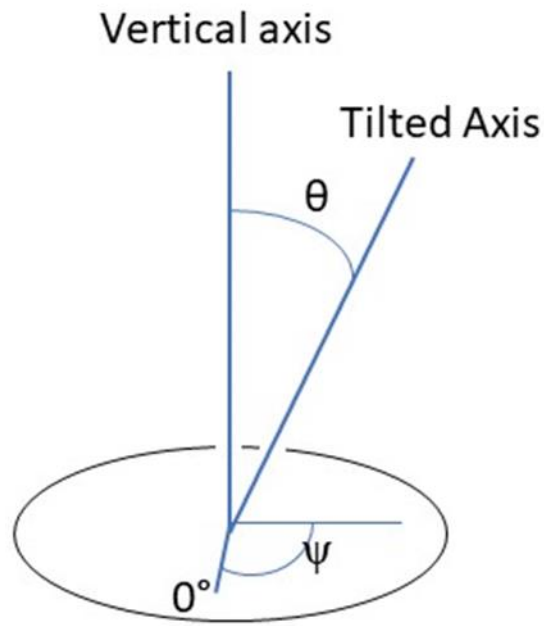
Figure 8: The coordinate system for the tilt angle analysis

Note that a base plate is installed to the concrete cylinder before undergoing

tomography. It can provide accurate alignment and the notches on edges can be

regarded as reference marks during image registration. (Serge 2019) The origin of the

coordinate system is located at the centroid of the interface between the bottom of the

concrete specimen and steel base plate. All centroids from each trial arrays from the

bottom to top in the order of height. As a result of data process, the tilted axis will not

perform like the one in Figure 7. Especially, the coordinates of centroids changes

from slice to slice which means that the centroids are not in the same x-z plane. To

overcome this problem, set a reference point to determine the displacement of the

centroid of the slice to vertical axis, which is given by:

$$r = \sqrt{(\Delta x)^2 + (\Delta y)^2}$$

Where r is the distance, Δx and Δy are the distances between the centroid of the

CT slice and the centroid of the base in x-axis direction and y-axis direction, respectively. Select a slice that can clearly perform the base plate and set its centroid as fiducial point. Note that the images acquired from tomography need to be filtered before doing calculation of tilt angle. Epoxy adhesive, a material with heat resistance and high stability, was used to stick the concrete cylinder and steel base plate together. The sealing film made by PTFE (polytetrafluoroethylene) was used to prevent the loss of water during the scanning. (Serge 2019). Due to two factors above, the images of the top of the cylinder and the images near the bottom of the cylinder will not be used because of their poor quality and resolution. Images that have been though the sifting process can be used for subsequent calculation. After finding all the distances between the reference point and centroid of each slice, organize these data in the order of height and do linear regression analysis using collected data. The angle between regression line and vertical axis is considered as tilt angle of the cylinder. Once the slope of the regression line is determined, the calculation of angle becomes a simple trigonometry problem. Since some slices that do not meet the requirements are skipped, the initial distance does not always equal to zero, which means that the regression line will not start from the origin point. However, this does not affect the slope of the trend line obtained.

Figure 9 is the plot of the centroid displacements for the three scans of DP1-3, the control specimen which did exhibit any expansion. It can be seen that DP1-3-4 and DP1-3-5 appear as straight lines. The third scan is curved and may be suspect because

of problems in finding the center of mass in this set of slides. It will be omitted from further discussion. The other two seem to be parallel. This can be tested by simply shifting DP1-3-5 vertically by 224 pixels as shown in Figure 9. The difference between two scans is due to the specimen being mounted in the NeXT system at different heights relative to the camera in the two successive scans. The complete overlap of the data points indicates that the two datasets could be pooled into a single one providing a total of 3,215 points for the linear regression analysis. This resulted in a very precise estimate of the tilt angle of $2.165 \pm 0.001°$. The fact that the tilt angle remained constant from one scan to another suggest that it was not due to the swelling of the epoxy during storage in the limewater bath. It is probably was introduced during the casting of the specimens or and epoxying of the specimen to the base.
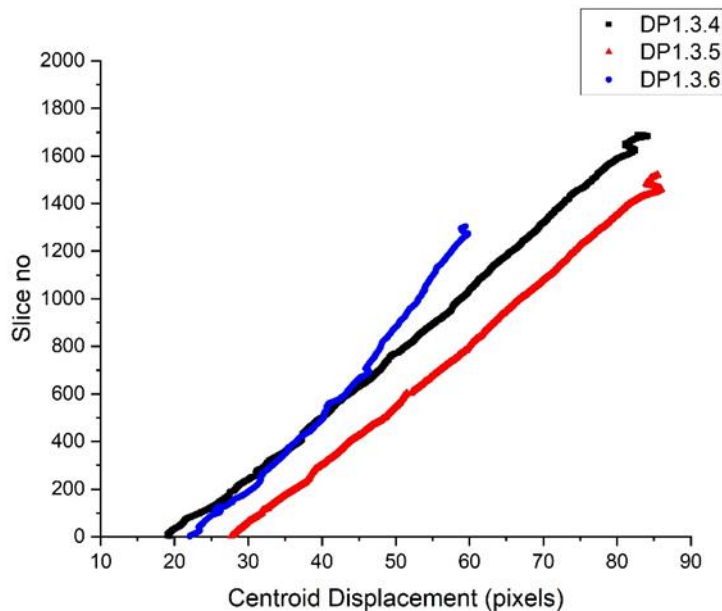
Figure 9: Plot of centroid displacements for the control specimen
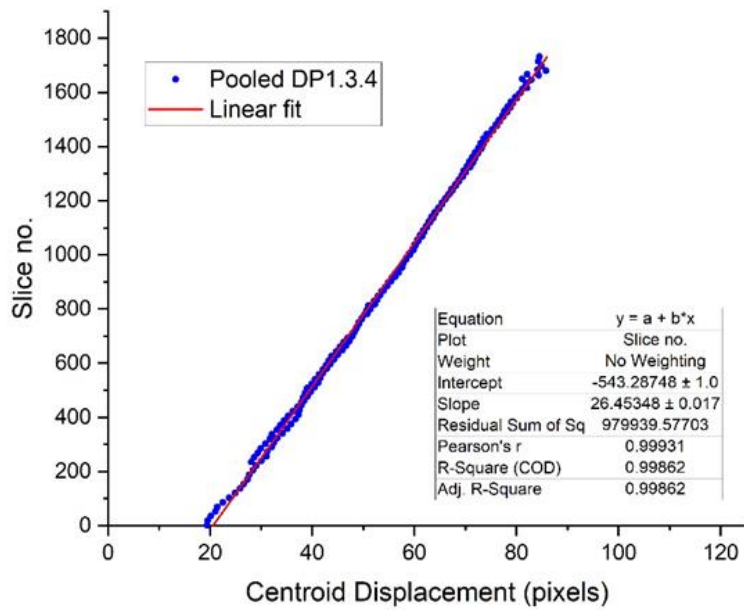
Figure 10: Linear regression analysis of pooled data for control specimen scan DP1-3-4

A similar analysis could not be carried out for the two heat-treated specimens because the deviations from linearity were too large as shown in Figure 9. The presents show the result of tilt analysis of these two concrete specimens. at 148 days after casting.

(a)

DP1-1-5   y = 44.948x - 67.28
           R² = 0.5528

(b)

DP1-1-6   y = 40.855x + 208.52
           R² = 0.293
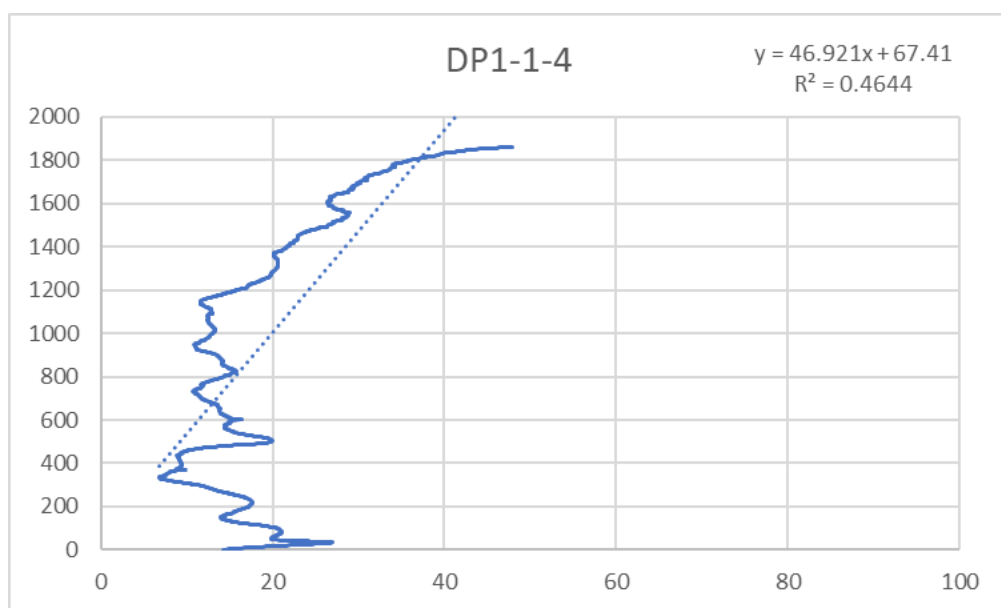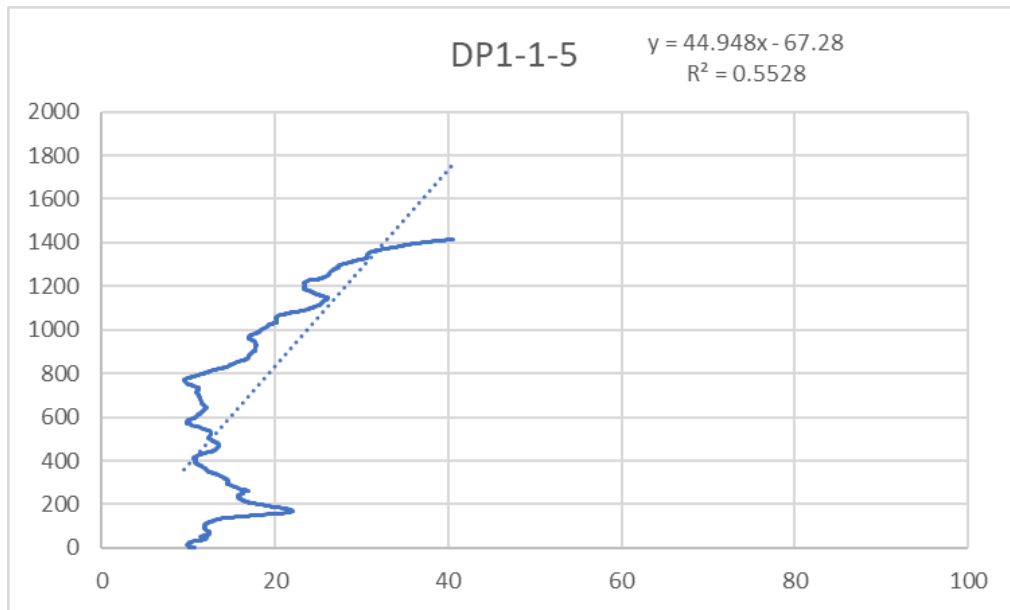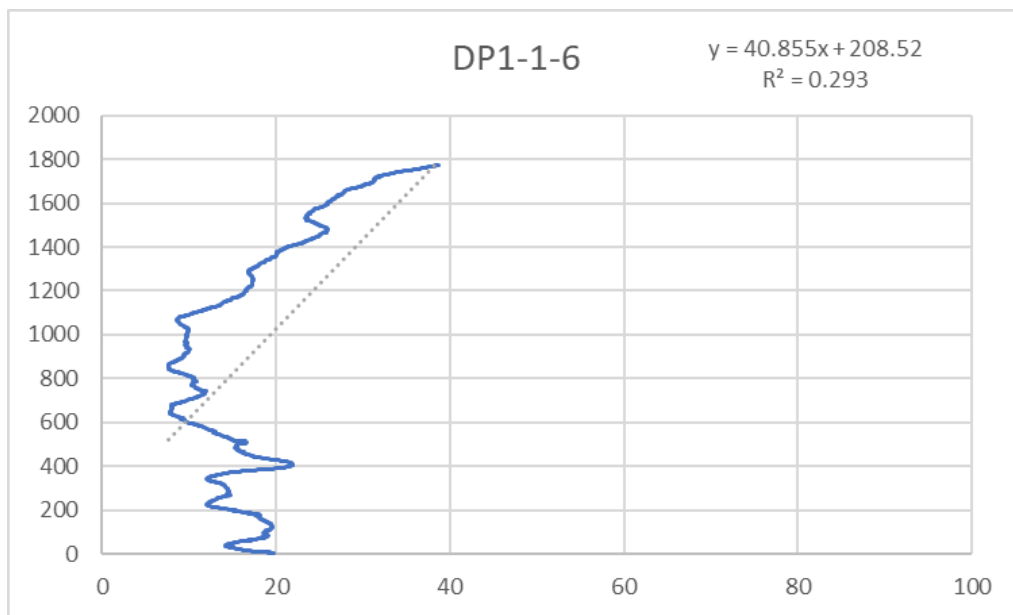
(c)
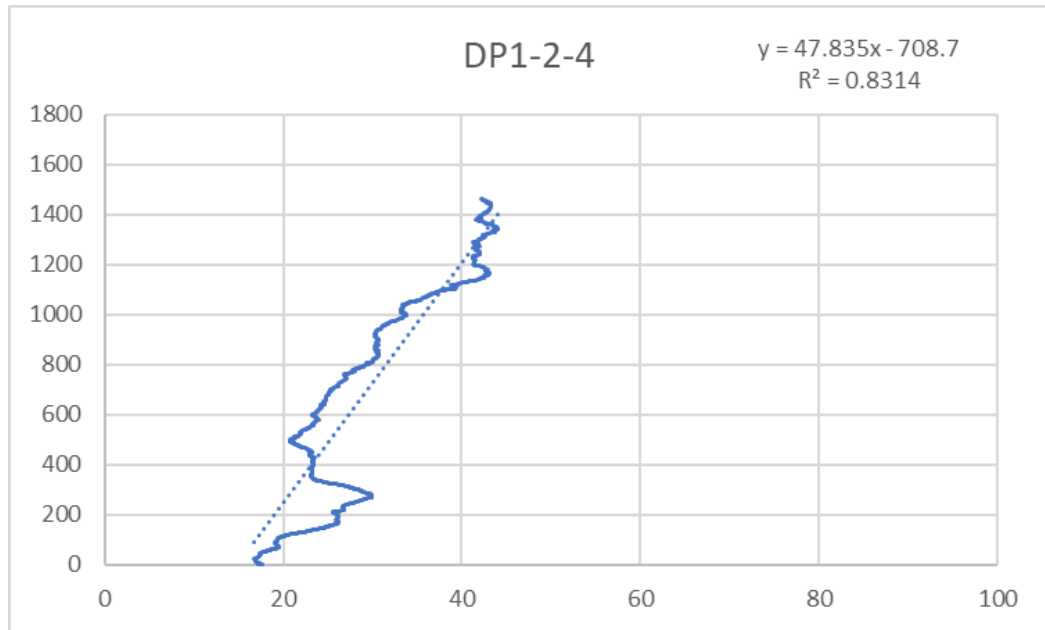
(d)
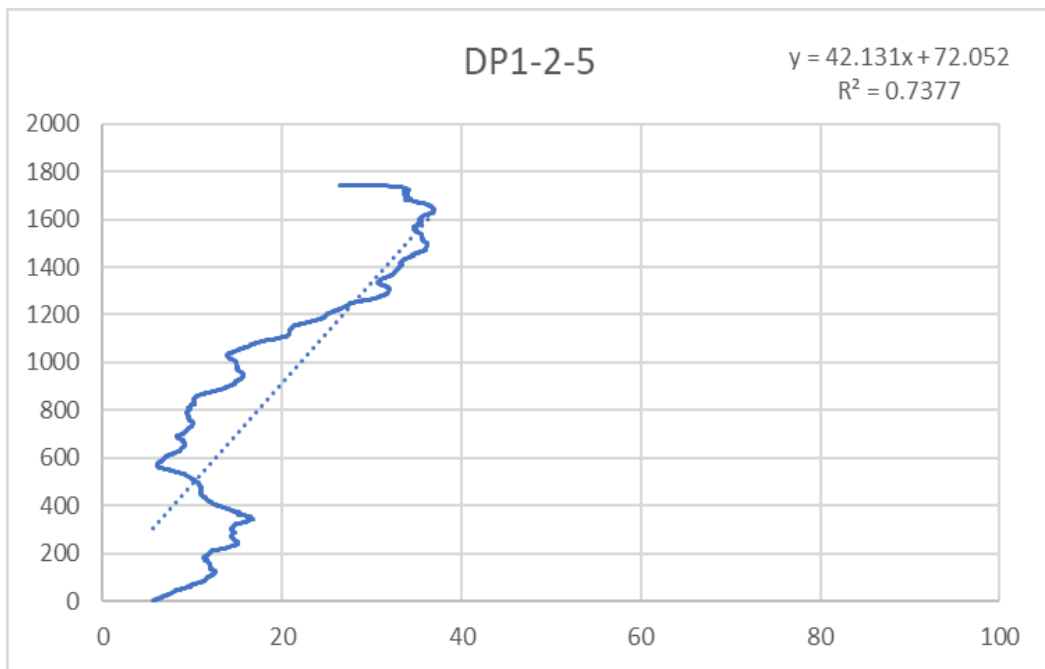
(e)
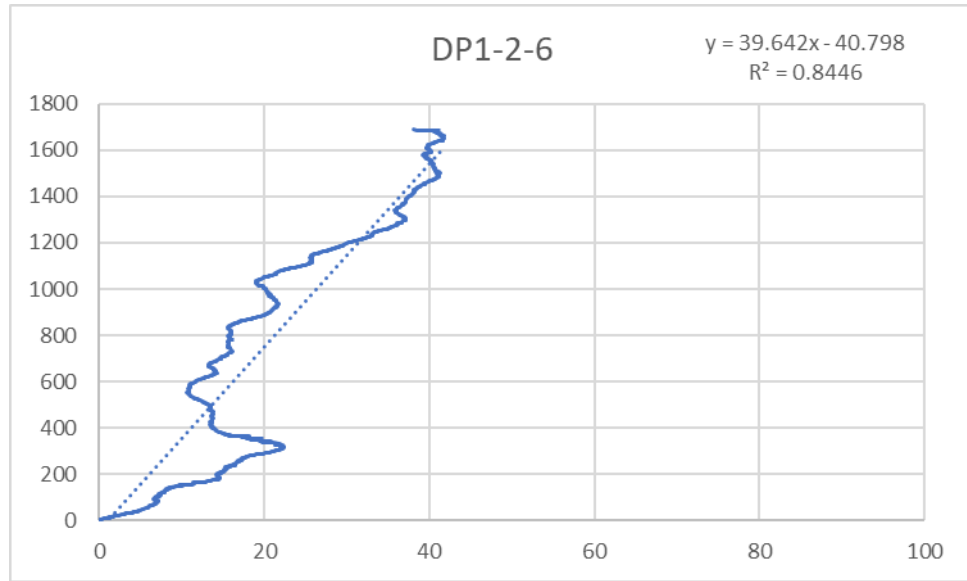
(f)

Figure 11: Result of tilt angle analysis. (a) to (f) represent the result of data of the heat-treated specimens.

The horizontal axis in the graph represents the distance between centroid of slice and reference centroid and vertical axis represents serial number of slices that determines the height of tomography. The unit of distance is pixel. Since the number of images obtained by each tomography is different, and the number of images discarded because of poor quality is different, the height in each result is also different. The equation of the trendline and the value of R-squared for each graph is shown on the right corner. The polylines in graph produced by first two sets is very tortuous and the R-square values of first two sets also illustrate that the regression line does not fit the data well.

Table 4: Tilt Angle

Serial Number	Equation of Regression Line	R-Square Value	Tilt Angle

DP1-1-4	y = 46.921x + 67.41	0.4644	1.22°
DP1-1-5	y = 44.989x + 84.708	0.553	1.27°
DP1-1-6	y = 40.855x + 208.52	0.293	1.40°
DP1-2-4	y = 47.835x - 708.7	0.8314	1.20°
DP1-2-5	y = 42.131x + 72.052	0.7377	1.36°
DP1-2-6	y = 39.642x - 40.798	0.8446	1.45°

Review the part in sample preparation, the specimens of set 1 and set 3 have normal level of potassium, the specimen of set 2 is with added potassium. Plus, set 3 is treated as control group with no further treatment. The time interval between the fourth and fifth tomography test, and the time interval between the fifth and sixth test are 46 days and 82 days, respectively. According to Table 4, the tilt angle given by the three groups of set 1 increases with time, and the difference between first and last angle is 0.18°. As for set 2, the tendency of the change of angles is similar to set 1. From fourth test to sixth test, the tilt angle has changed for 0.25 which is larger than the corresponding value of set 1. The tilt of set 3 might be caused by the partial slumping. The result of the DP1-3-6 data are significantly different from those of other two sets of data. Tilt angle of DP1-3-6 has a sudden drop. After repeated verification with existing methods, the result remained the same. The likely cause of this happening is due to the reason of the tomography technique or the sample itself got changed during the time interval. The consistency of regression lines of three different sets is different. The R-square value of first set is around 0.4 which is

relatively low. Set 2 has value approximately 0.8.

Table 5: Regression Analysis

Serial Number	Coefficients and Intercept	Standard Error of Coefficients and Intercept	Standard Error
DP1-1-4	+46.92 / +67.41	1.17 / 23.36	393.34
DP1-1-5	+44.99 / +84.71	1.44 / 27.02	378.31
DP1-1-6	+40.89 / +208.45	1.51 / 27.00	429.80
DP1-2-4	+47.84 / -708.596	0.56 / 17.58	173.5328
DP1-2-5	+42.09 / +73.26	0.60 / 13.01	257.93
DP1-2-6	+39.64 / -40.91	0.41 / 10.38	192.23
DP1-3-4	+26.69 / -554.38	0.07 / 4.15	56.06
DP1-3-5	+26.10 / -745.31	0.02 / 1.30	14.16
DP1-3-6	+34.80 / -848.77	0.10 / 4.56	39.74

This table includes the standard error of coefficient and intercept which interpret the precision of the regression analysis. The smaller number of standard errors represents the regression equation more reliable.

Each time the tomography produces 1800 to 2200 images. After removing nonconforming images, there are still 1400 to 1800 images to be processed. It is impossible to check the results slice by slice to determine whether the algorithm is appropriate or whether there are factors that could cause errors. The current algorithm is only able to calculate the center of mass of an enclosed figure without any holes

inside. In order to get the centroid of the slice conveniently, the voids in the cylinder are filled up during the calculation. This will lead to the deviation of the desired center of mass from the actual result. Despite having image cleaning process, some unexpected residues outside the shape may still be involved in calculation of centroid. The large horizontal deviations in the two heat treated specimens indicate a shear strain caused by non-uniform expansion with height. Their magnitudes are comparable to the variances of the mean radius.

- *Polar Plots*

Generating a polar plot of centroids of the slices is another approach to illustrate tilt of the cylinder. Knowing the tilt angle of the cylinder, the movement and the rotation of the centroid of the slice on the horizontal plane becomes the next topic. In order to clearly show the trajectory of the movement of centroids in the horizontal plane, gather all recorded centroids in a polar coordinate system. Keep the center of the steel base plate as the origin of the coordinates. All centroids of slices disperse around the origin according to their radial distances from origin and azimuth angles. Figure 12 shows polar plots of all three sets.

(a) DP1-1-4

(b) DP1-1-5

DP1-1-6 Polar plot of Scatter points of centroid point

(c) DP1-1-6

(d) DP1-2-4

DP1-2-6 Polar plot of scatter points of centroid point
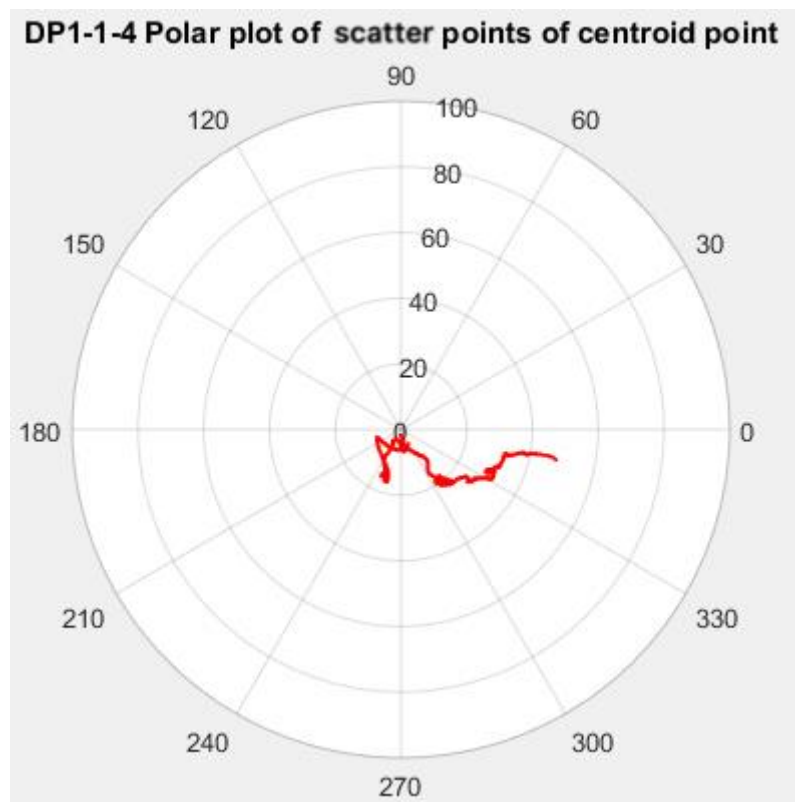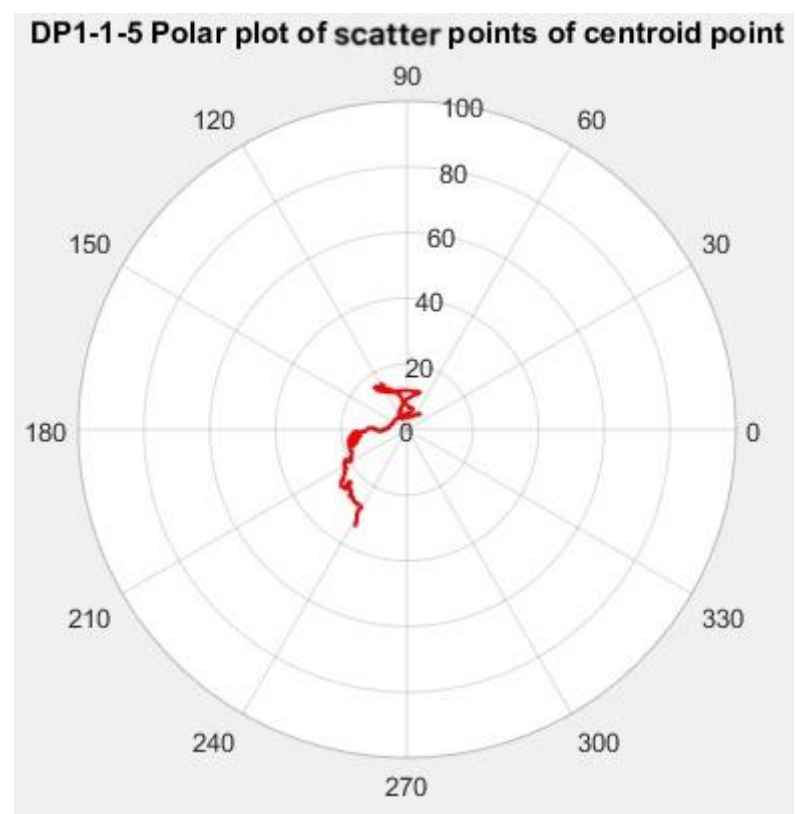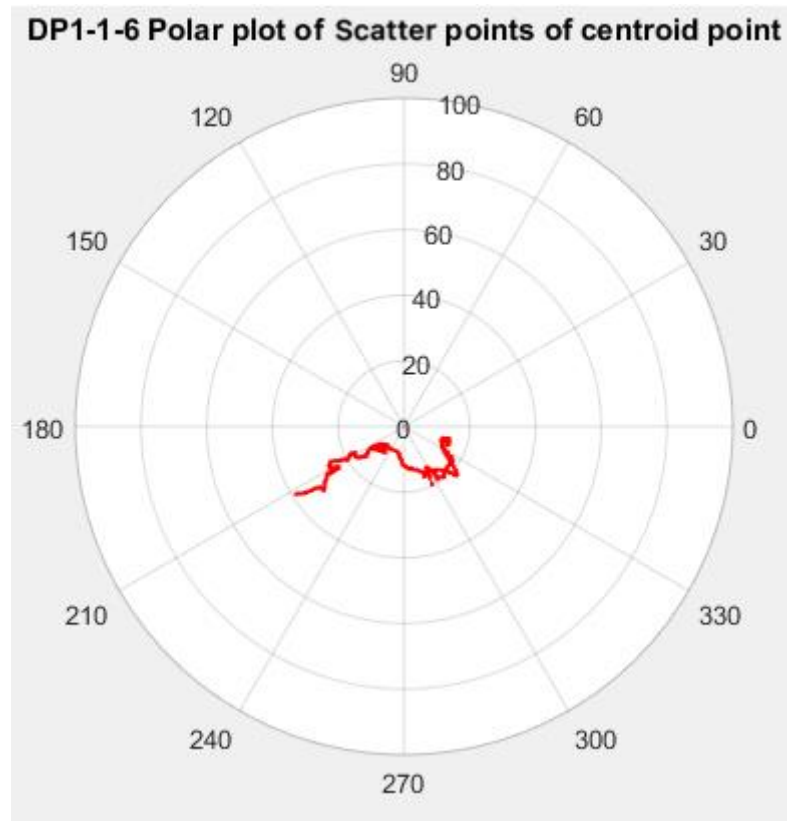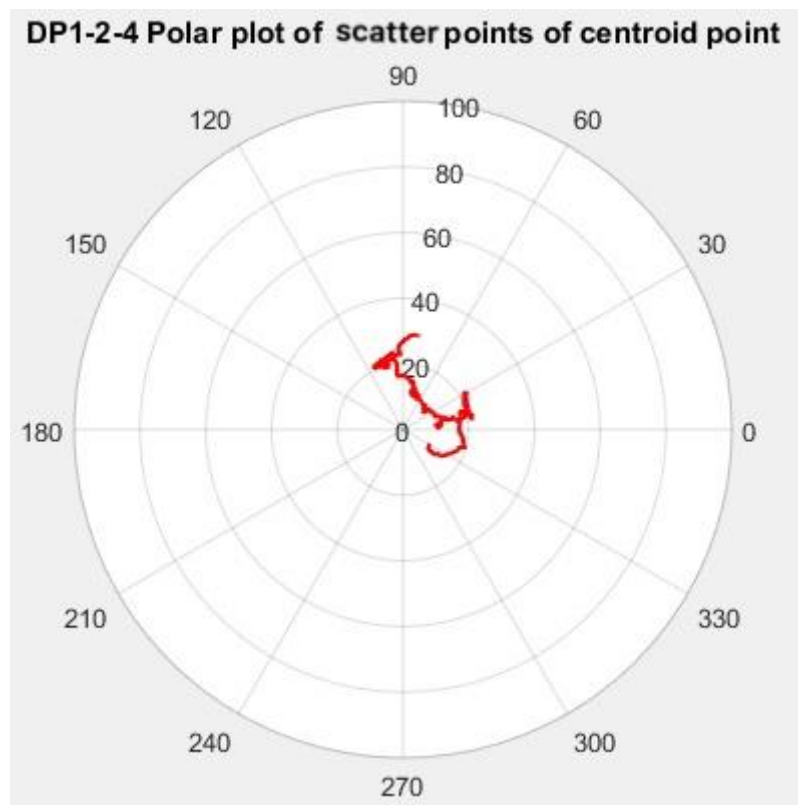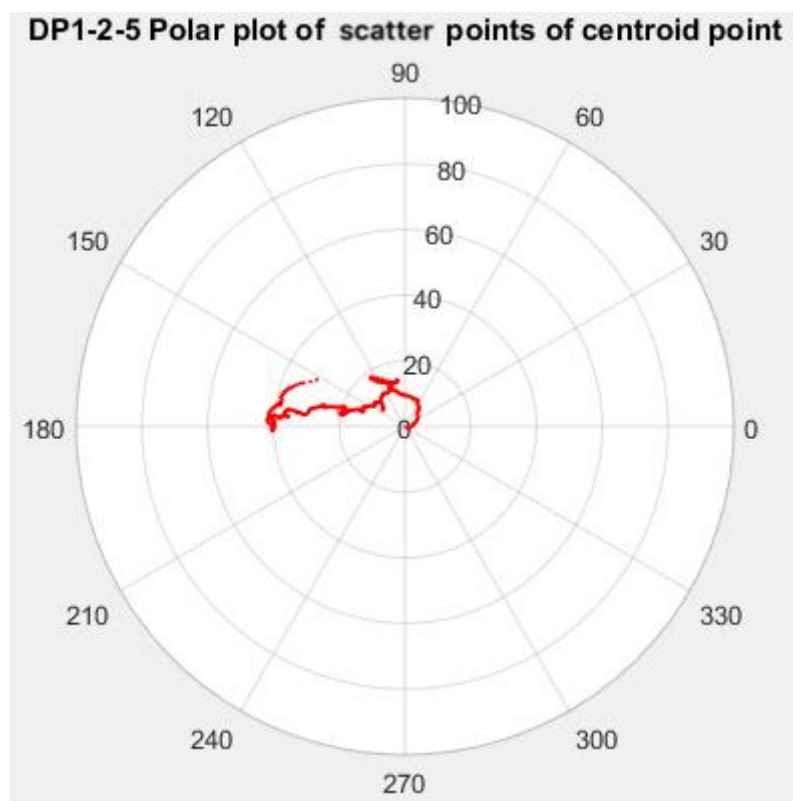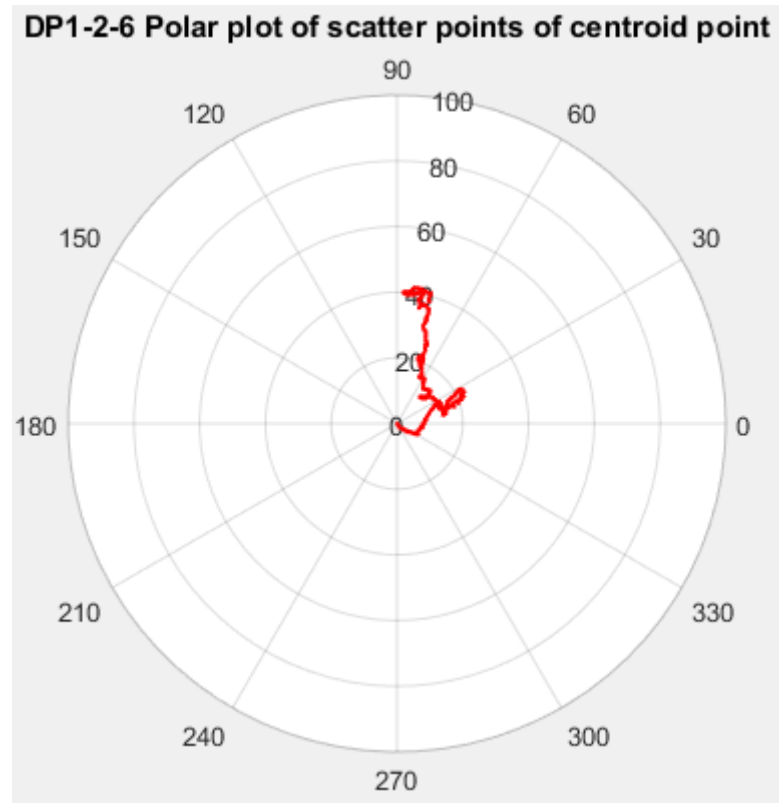
(f)

DP1-3-4 Polar plot of scatter points of centroid point
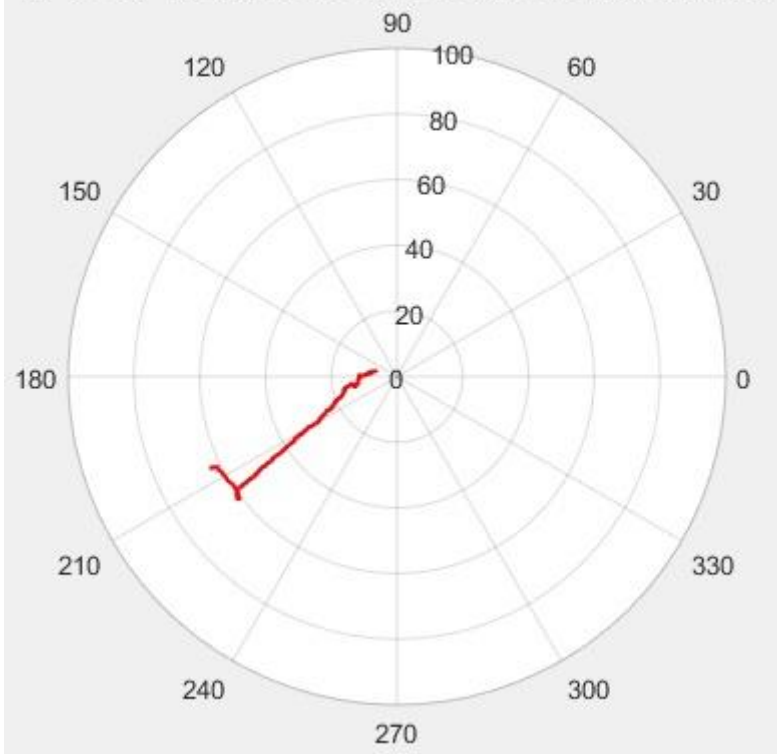
(g)

DP1-3-5 Polar plot of scatter points of centroid point

38

(h)

DP1-3-6 Polar plot of scatter points of centroid point
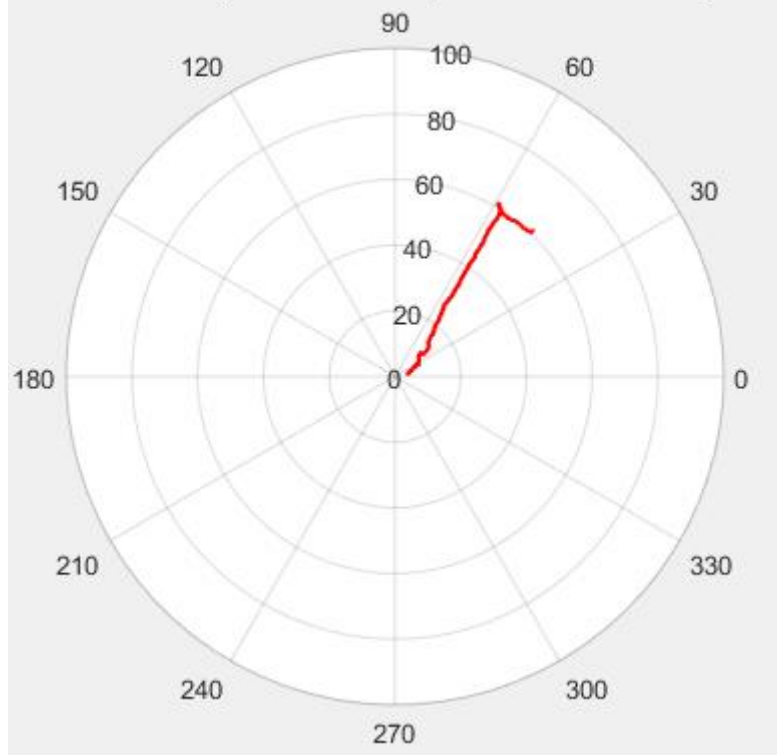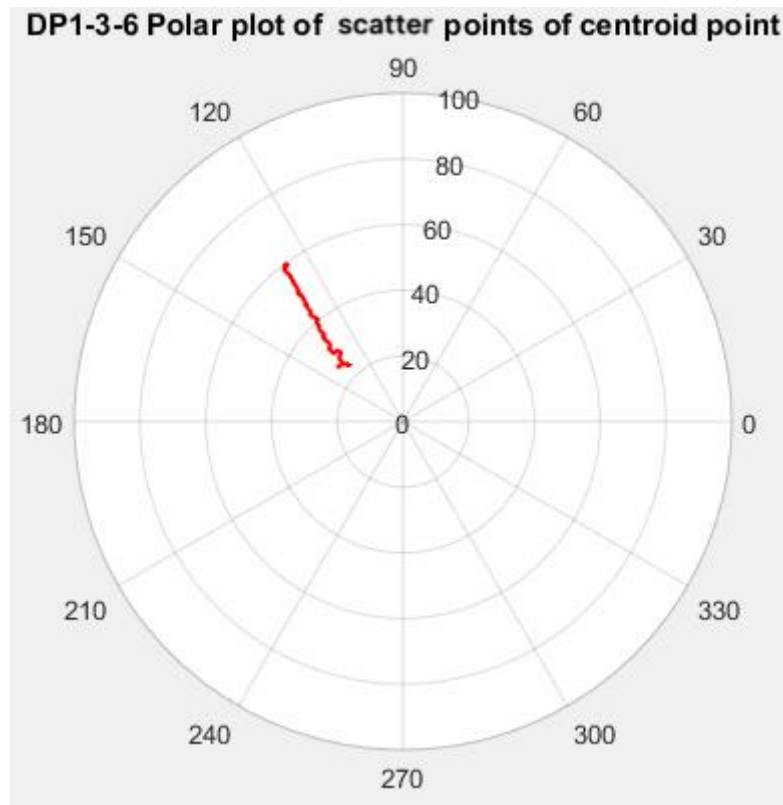
(i)

Figure 12: Scattered centroids in polar coordinates (a) to (i) corresponding to DP1-1-4 to DP1-3-6

Vertical array of numbers denotes the distance from the origin and the unit is pixel.

In the figures, the centroids are gradually deviating from the origin as the height growing. Ignoring the error of the last part of the data, the centers of slices in each trial of set 3 almost forms a straight line, which shows that the axis of the set 3 can be considered as a straight line with an angle to perpendicular. In figures of set 1 and set 2, the trajectory of movement of points is more irregular than that of figures of set 3. There are many changes in the direction of the point movement which is why the distance plot fits the trend line to a lesser degree for set 1 and set 2 when generating

the tilt axis of the cylinder. The azimuth angle also varied from one slice to another, a sign of twisting.

Calculation of tilt angle and polar plots have proved that some changes have taken place inside the concrete cylinder specimens, which results in the axis of the cylinder not forming a straight line in space. Comparing with the control group, the internal differential expansion could be the reason why the axis becomes tortuous. One thing that can be ascertained is that after concrete cylindrical specimens of set 1 and set 2 undergo thermal cycling and special treatments, inhomogeneous internal expansion occurs. The expansion makes the centroid of the shape deviate from original axis. As for the tilt, the tilt angles of set 1 and set 2 have a tendency of raising. However, it is not likely that a reliable conclusion can be drawn from the relationship between the time series and the tilt angle of the cylinder sample. On the one hand, regarding the regression line as the axis of the cylinder, the angle obtained from the regression line is not convincing because the fitting degree of the data to the trend line is not high. On the other hand, the performance of EPOXY used to glue the base plate and the possible tilt of the mold of the concrete specimen can interfere with the process of determining tilt angle. In future experiments, eliminating these interference factors will be helpful to get more accurate and reliable results.

Chapter 5. Microbead Analysis

The three different kinds of microbeads placed in the concrete specimen during casting are intended primarily for calibrating the grayscale histograms. They can also serve as reference points for the process of image registration. Finally, the variation in height and position of the microbeads from one scan to another could be helpful in studying the local displacements over time that may be caused by DEF.

The first step in the microbead analysis is to identify them in the reconstructed 3 D volume. This is done by an image processing method known as template matching. This takes advantage of the fact that the microbeads have characteristic values of size, circularity and attenuation factor that can be used to distinguish them from other features in the CT image.   The image of Each microbead is composed of several contiguous pixels with a specific pattern gray scale value. This is used to create a 32x32 or 44x44 array known as a template or mask. This template can be compared to a similar-sized array of pixels at a point in a CT slice to determine if there is a good match. The degree of matching is typically evaluated by some type of cross-correlation coefficient (Shapiro 1993). The template is then moved to the next position of the image and the cross-correlation function is recalculated and recorded.

The Normalized Cross Correlation (NCC) is a conventional template matching algorithm. The advantage of this algorithm is its strong white noise rejection capability, and robust accuracy against grayscale changes and geometric distortion. The position at which the correlation coefficient is the largest determines the

coordinate of the template image in the target image. The formula for the NCC

algorithm is (Yoo 2009):

$$\gamma(u, v) = \frac{\sum_{x,y}[f(x, y) - \bar{f}_{u,v}][t(x - u, y - v) - \bar{t}]}{\{\sum_{x,y}[f(x, y) - \bar{f}_{u,v}]^2 \sum_{x,y}[t(x - u, y - v) - \bar{t}]^2\}^{0.5}}$$

Where *f(x, y)* is the image pixel intensity at point x, y; *t(x, y)* is the template pixel

intensity at *x, y*; *u* and *v* are shift variables for *x* and *y* respectively; *t* is the mean of

the template and $\bar{f}_{u,v}$ is the mean of *f*(x, y) in the region under the template.

In this study, the images of the three types of microbeads are defined as the

criteria, and their specific pixel values are set as templates for subsequent searching

procedures. There are two matrices required for calculation: the matrix containing the

all pixel values of the template and the matrix containing all pixel values of the slice.

The matrix of microbead always has a smaller size than the matrix of the slice. After

computing the normalized cross-correlation of matrices of microbead and slice, the

correlation coefficients ranging in value from -1.0 to 1.0 form a new matrix. The

dimension of the new matrix is the sum of the dimensions of the template and the

image. To filter these coefficients, a threshold is set based on the valid data of

microbeads. The calculation of this 2-dimensional NCC is done in MATLAB.

The materials of microbeads were selected to have attenuation coefficients that

would provide strong contrasts in the CT images relative to the various concrete

phases Table 6 contains the theoretical neutron and X-ray attenuation coefficients of

the three materials. These values are also with the concrete phases in Figure 13.

Table 6: Attenuation Coefficient

	Attenuation Coefficient, cm^{-1}	
Type of microsphere	Neutron	X-Ray
Stainless steel	1.2	21.4
Barium titanate	2.2	61.44
Polystyrene	4.2	0.21
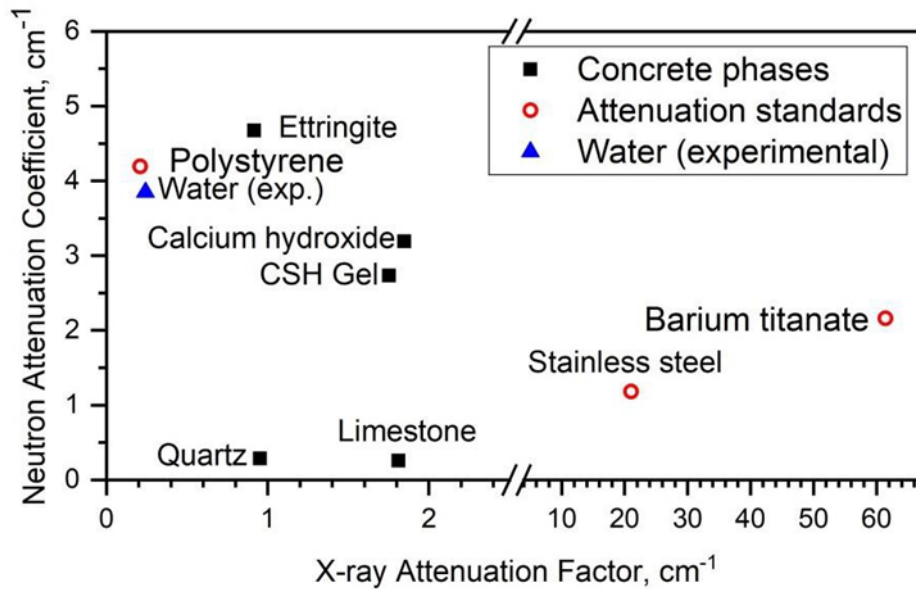
Figure 13: Bivariate plot of neutron and X-ray attenuation coefficients for the concrete phases and the microbead attenuation standards

The barium titanate or stainless-steel microbeads have X-ray attenuation factors that are higher than all the other materials and therefore would stand out in the X-ray image. However, the neutron factors are much lower than the hydrous concrete phases and thus they would be difficult to detect in neutron images. Conversely, the polystyrene has an X-ray attenuation factor that is similar to the other phase and hence it would not be possible to find it int the X-ray images. It should be noted that values

in Table 6 and Figure 13 are calculated using single values of neutron and X-ray energies, 25.3 MeV and 45 keV respectively, but both types of radiation would have a range of energies in the actual concrete specimens. Consequently, the actual absolute values of the attenuation factors may be different, but the relative positions in Figure 13 would remain the same.
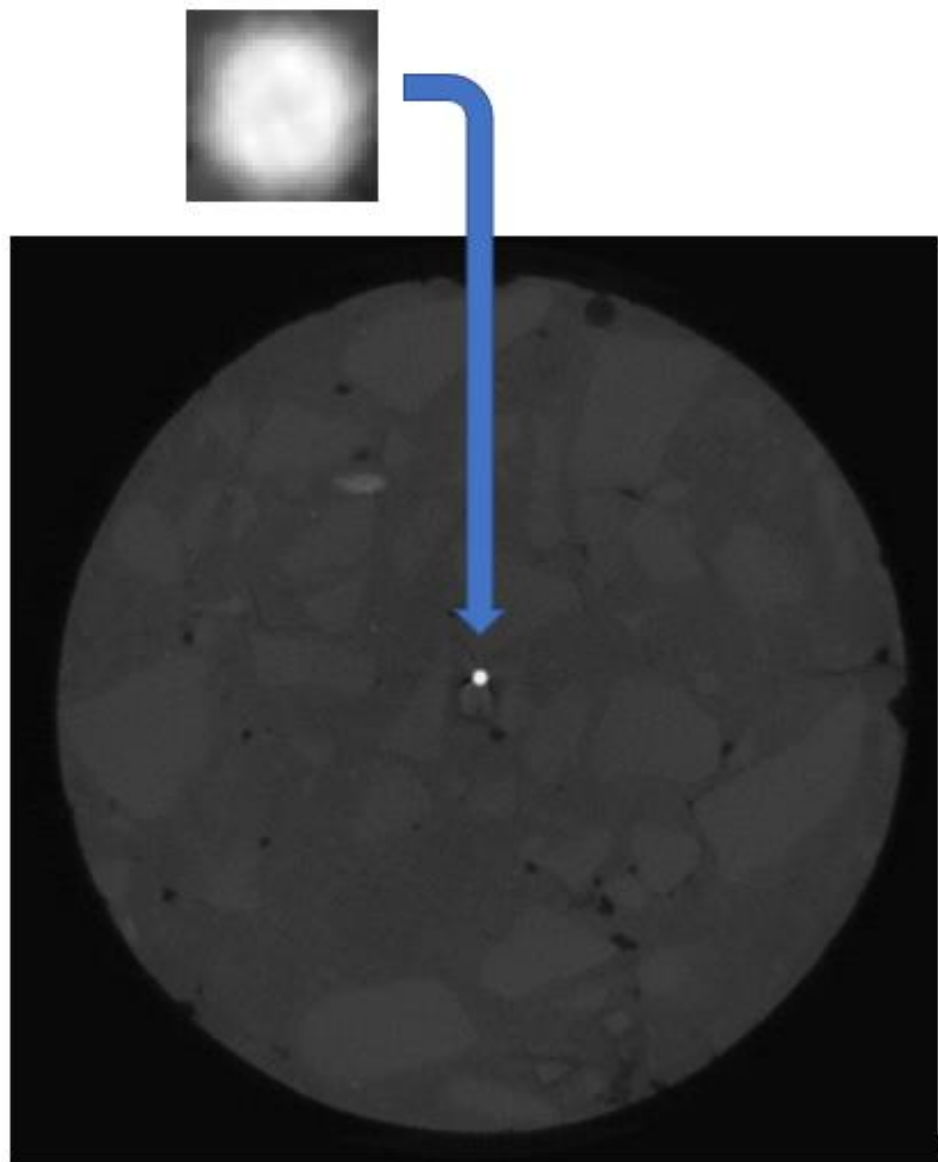
(a)
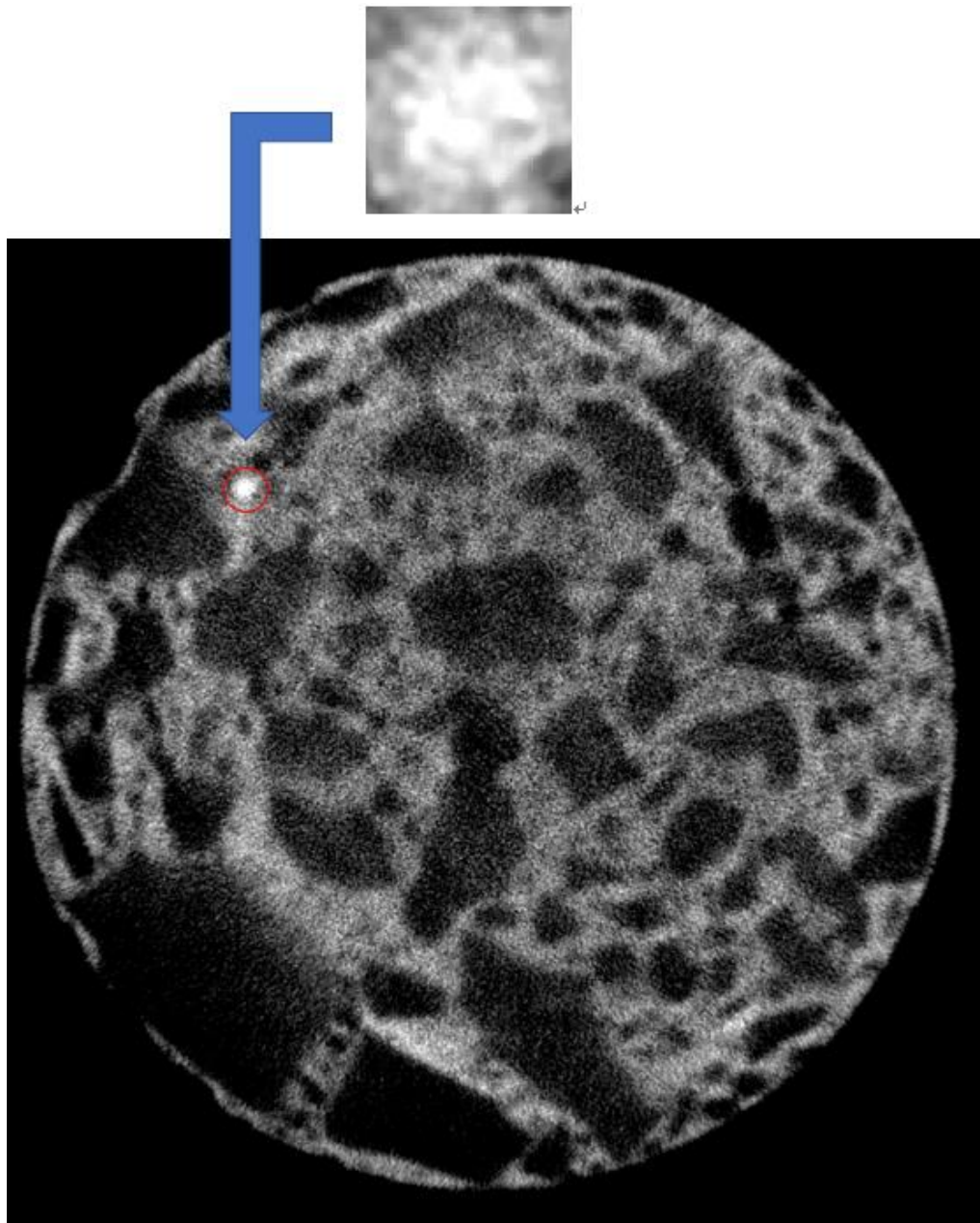
(b)

Figure 14: Templates of microbeads found in slices. (a) is X-ray image; (b) is neutron image

Figure 14 illustrates the process for manually setting up the templates using slices in which microbeads had been selected by visual inspection. The image processing program Image J is used for adjusting the brightness of the slice and then for cropping a square template from it The x-ray image clearly shows the position and grayscale

contrast of the stainless steel microbead The polystyrene bead in the neutron image is

harder to distinguish because of the lower contrast.

1.011   2.531

Count: 1936   Min: 1.011
Mean: 1.878   Max: 2.531
StdDev: 0.263   Mode: 1.827 (36)
Bins: 256   Bin Width: 0.00593

(a)

0.816   7.232

Count: 1024   Min: 0.816
Mean: 4.480   Max: 7.232
StdDev: 1.935   Mode: 6.693 (20)
Bins: 256   Bin Width: 0.0251

(b)

46

Count: 1024   Min: 1.197
Mean: 7.030   Max: 11.502
StdDev: 3.117   Mode: 11.361 (16)
Bins: 256   Bin Width: 0.0403
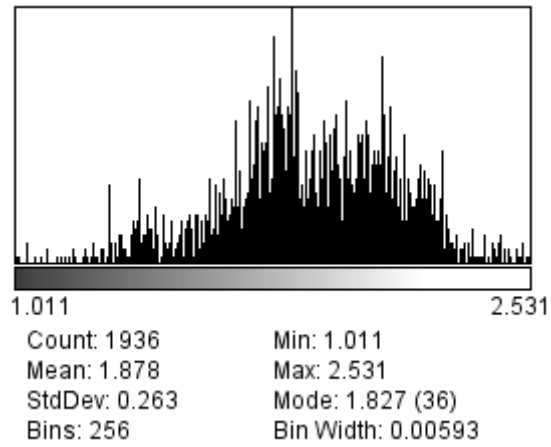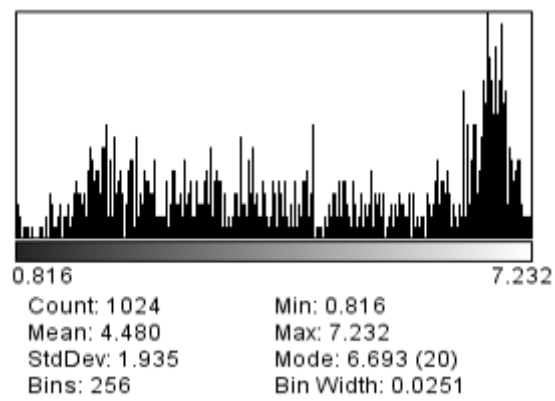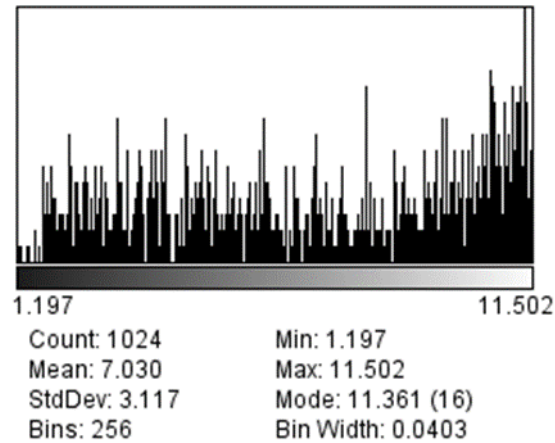
(c)

Figure 15: Grayscale histograms of the microbead templates: (a) Polystyrene; (b) Stainless steel; (c) Barium titanate

The grayscale histograms for the microbead search templates are displayer in Figure 15. The mode values are the most probable. They are 2.51 for polystyrene, 7.23 for stainless steel and 11.5 for barium titanate. These are all lower than the predicted theoretical values. This indicates that the actual neutron and X-ray photon energies in the concrete were higher than the ones used in the calculations.

The threshold value of the correlation coefficient for positive identification of the microbeads of the is different for X-ray image and neutron image due to the difference in resolution between the two modes. After some trial and error, it was determined that the most effective threshold value is 0.90 for the X-ray images and 0.7 for the neutron images. With the thresholds set at these values, all the microbeads can be correctly found. Figure 16 (a) and (b) illustrate this process. The location of microbead shown in Figure 16 (a) and the values of the cross-correlation coefficient as a function of position are displayed as a surface in the 3-D plot, in Figure 16 (b).

However, there is the possibility that this automated method will also produce false positives due a random cluster of pixels aliasing the microbead pattern. The error can be eliminated by visual inspection.

Another limitation of this method Is the problem of resolving the individual microbeads when two or more are close together. due to the mutual interference of the grayscale This can result in the incorrect identification of only a single microbead or a false negative of microbeads. Those microbeads that this algorithm fails to find need to be detected manually through Image J.
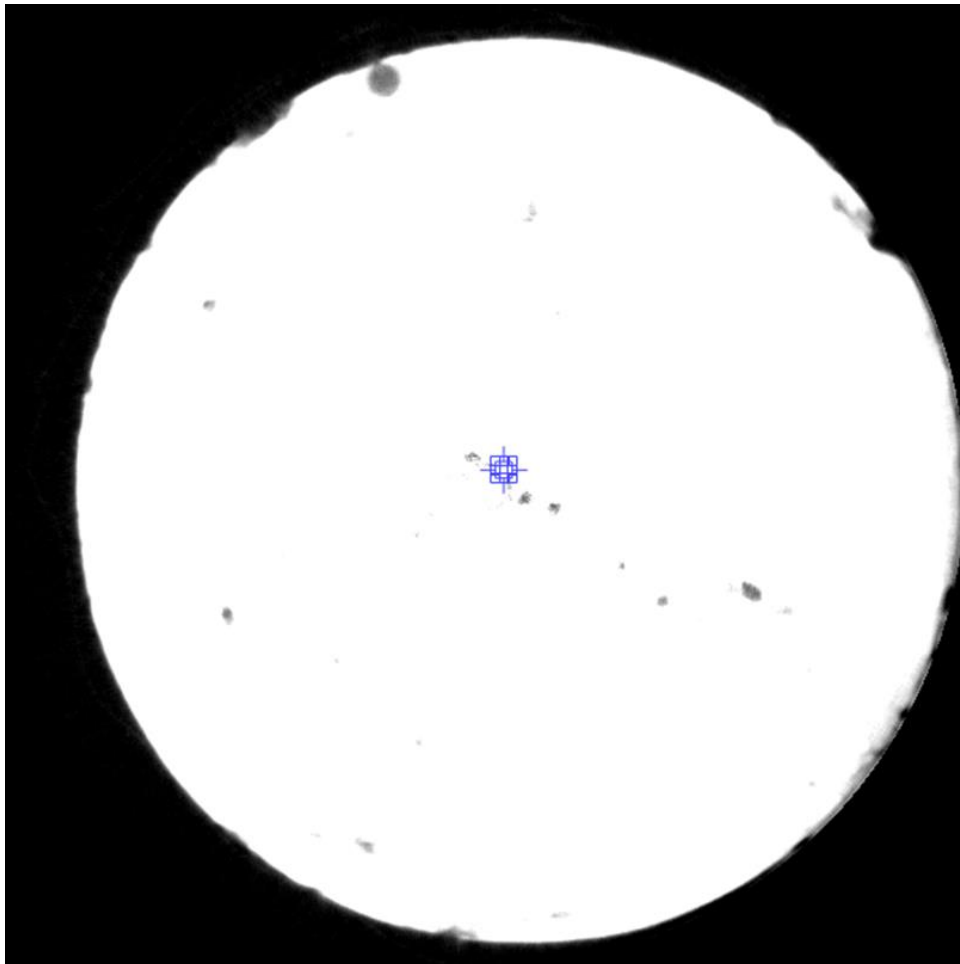
(a)
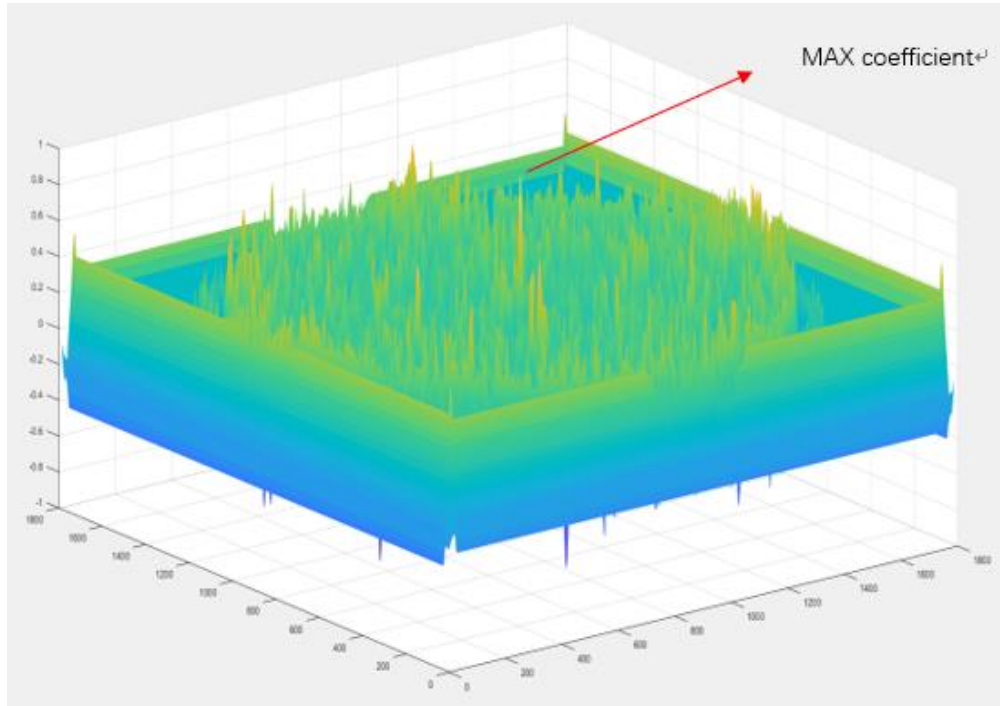
(b)

Figure 16: (a) the matching result of slice shown in Figure 14 (a); (b) Plot of the NCC

correlation coefficient as a function of position in the image.

The position coordinates of the individual microbeads that were detected by the

NCC algorithm are presented in Appendix B. The results of the NCC searches for the

microbeads is summarized in Table 7.

Table 7: Results of Microbead Searches

Set NO.	Embedded microbeads		Number detected		
	Material	Number	Scan 4	Scan 5	Scan 6
Set 1	Polystyrene	5	1	1	0
	Barium titanate	5	5	5	5
	Stainless steel	8	8	8	8
Set 2	Polystyrene	5	0	0	0
	Barium titanate	5	5	5	5

	Stainless steel	~9	8	8	7
Set 3	Polystyrene	~5	1	0	0
	Barium titanate	6	6	5	5
	Stainless steel	9	9	9	9

Due to the limitations of the NCC method discussed above it was not possible to detect all the microbeads T There will always be some microbeads missing primarily the polystyrene ones. The main reason is the poor contrast of neutron image.

Chapter 6. Analysis of Void Ratio of Concrete Specimens

The void ratio is an important statistic of the materials properties of concrete because it influences the compressive strength. Also, the variation over time can be a measure of the progress of various reactions that generate products that can fill the void space such C-S-H gel or ettringite crystals.

In principle it should be relatively simple to quantify the fraction of void pixels in the CT image because these appear as a distinct at the end of the gray scale histogram as shown in Figure 17. This is a histogram of the grayscale values of a typical CT slice which was computed by the open source software Image J.
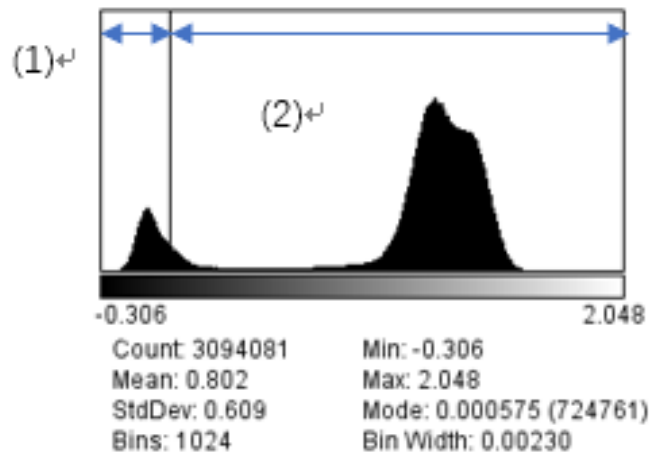

Figure 17: Histogram of a slice

The horizontal axis represents the pixel grayscale value, which in this case corresponds to the attenuation factor, divided into a set of bins, and the vertical axis represents the pixel count for that grayscale bin. For better resolution of the peaks, the number of bins is set at 1024. The peak centered around zero contains the void pixels

since the radiation passing through these pixels would experience no attenuation. The larger feature in the range of roughly 0.9 to 1.7 consists of multiple overlapping peaks made up of the pixels of the non-void phase of the concrete.

Theoretically, the void pixel peak should simply be a rectangle centered at 0 with a height equal to the number of void pixels and a width equal to the bin width of 0.0023. However, as can be seen in Figure 17, the actual shape is more complicated. In addition to the line at 0 which is the expected rectangle, the peak has both positive and negative wings. These can be explained with the help of some profiles presented in Figure 18 (a) and (b). The profile in Figure 18 (a) goes from the center of a void to the surrounding solid material. Many of the pixels in the void region have slightly negative values. This is an artefact of the image preprocessing, which involves subtraction of background noise. The profile also shows that there is not a step change at the wall of the void, but rather a gradient. This is caused by fact that the pixels in this gradient actually contain mixtures of void and solids in varying proportions. These mixed pixels make up the positive wing of the void peak in Figure 17.

The profile in Figure 18 (b) travels across the boundary between the interior of the shape to the exterior region. This show that the exterior points can also have negative or zero values. When calculating the proportion of voids in slice, these pixels need to be excluded.
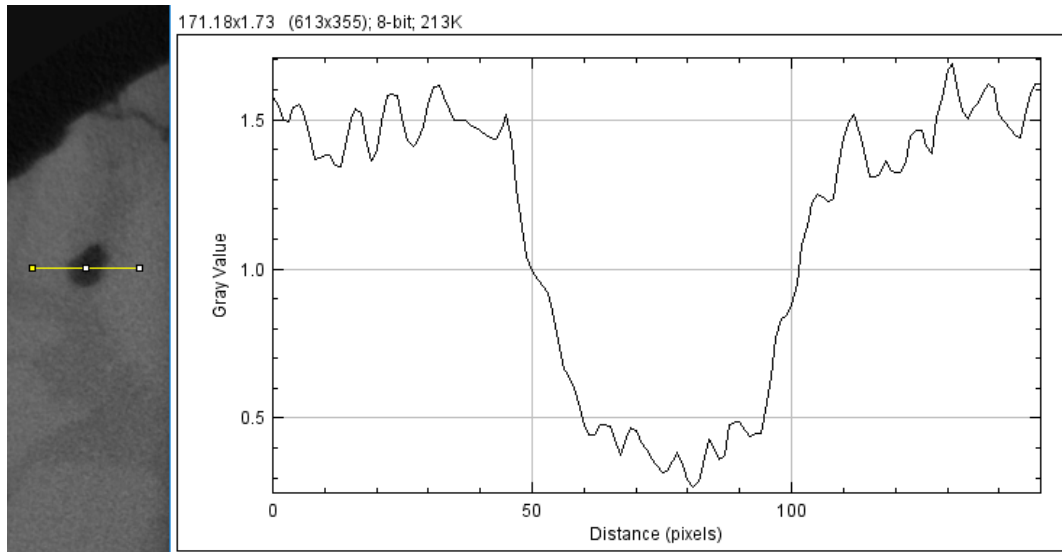
(a)
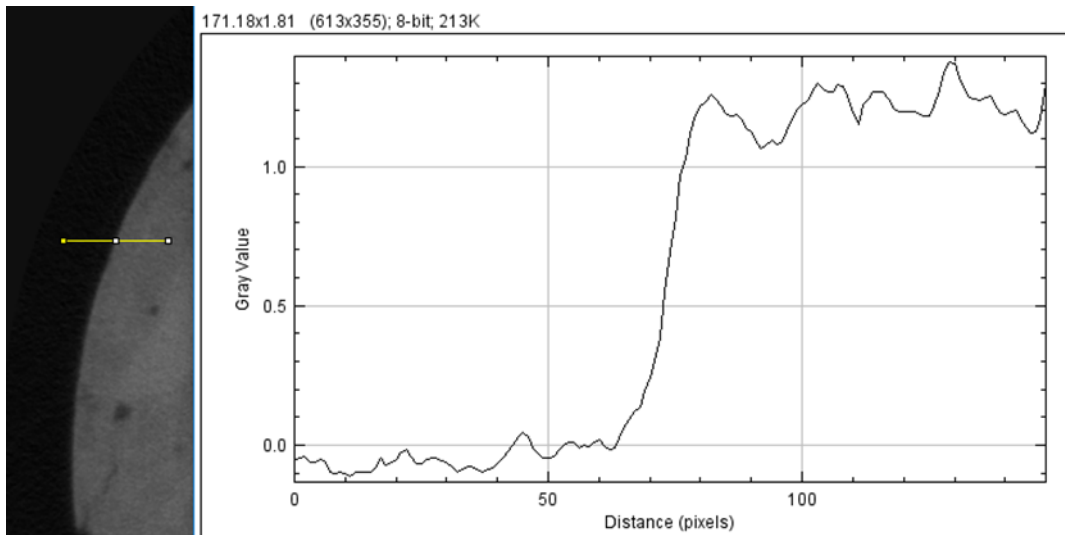
(b)

Figure 18: (a) Profile of void inside cross section; (b) Profile of interface between interior and exterior

This is accomplished by finding the coordinates of the boundary pixels and then counting only the void pixels only within those limits.

Setting the upper bound on the void segment of the gray scale histogram was further complicated that the overall grayscale tended to shift from one image to another. Consequently, the upper bound of the void segment fluctuated around the value of 0.8

reaching a maximum value 0.87. Therefore, the upper limit of the segment was set

conservatively 0.9 for all the slices.
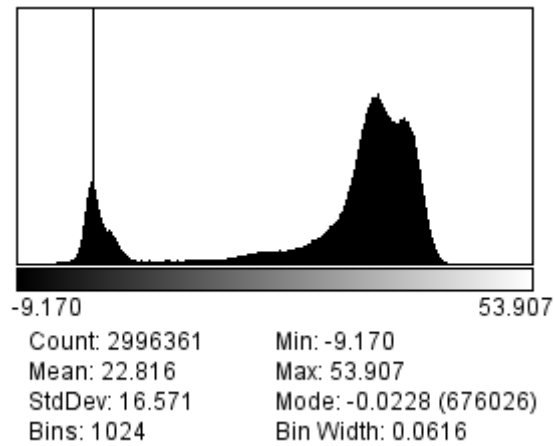
Figure 19: Histogram of a slice of DP1-1-6

It was necessary to exclude the data from DP1-1-6 from the analysis because of the

anomalous values of the gray scale histogram. This is illustrated by Figure 19 which is

the histogram of a randomly selected slice of DP1-1-6. The limits of its gray scale are

-9.17 to 53.907 where the normal gray scale ranges from -1 to 8. It is not clear why this

phenomenon occurred. It may have been an error in the preprocessing of the images

prior to the reconstruction of the 3-D tomography.

The workflow for calculating the volumetric void ratio proceeds by calculating the

gray scale histogram of an individual slice and counting the number of pixels that fall

into the range of the void segment. This sum is then divided by the total number of

pixels in the histogram to obtain the void area ratio for the slice. This process is then

repeated for the SNXC slice in the stack until the void area ratios for all the slices have

been computed. These are then averaged to give the mean void ratio for the entire

volume of the specimen. This is the equivalent of the number of void pixels in the

specimen divided by total number. The result is presented in Table 8.

Table 8: Mean Volumetric Void Ratios

Sample	Scan Number	Voids Ratio %	Mean	Standard Deviation
DP1-1	4	2.64	2.67	0.03
	5	2.69		
DP1-2	4	2.4	2.13	0.19
	5	1.98		
	6	2.02		
DP1-3	4	2.13	2.21	0.12
	5	2.37		
	6	2.12		

The void ratio of the three specimens s ranges between 2 and 2.6% percent with absolute uncertainties on the order of 0.1-0.2%. There seems to be no trend over time for the individual specimens.

Finally, the variation of void area ratio versus height s is presented in Figure 20 for the three specimens at scan number 5. The most prominent features for all three are the long tails at top and bottom which tend towards a significantly higher void ratio. The bottom is result of constraints on the packing of the aggregates against the bottom of the mold, and incomplete filling paste at the top. As for the middle part of the cylinder, the void ratios of all three shows some variation but no trend with height.
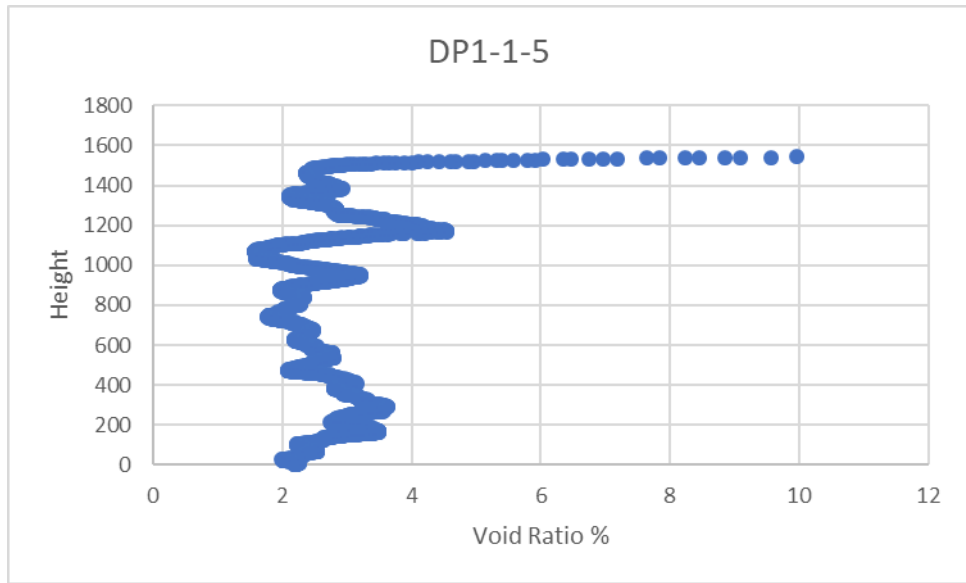
(a)
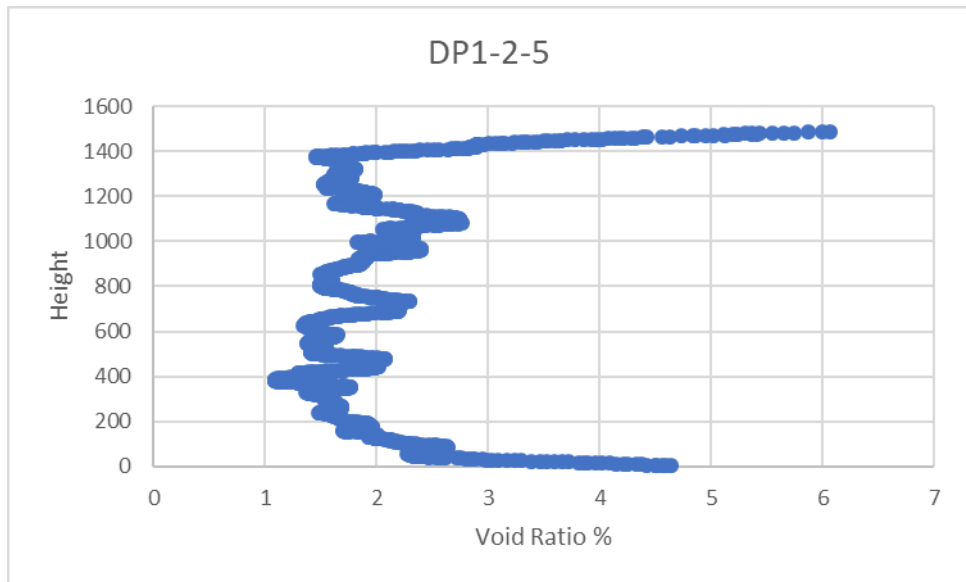
(b)
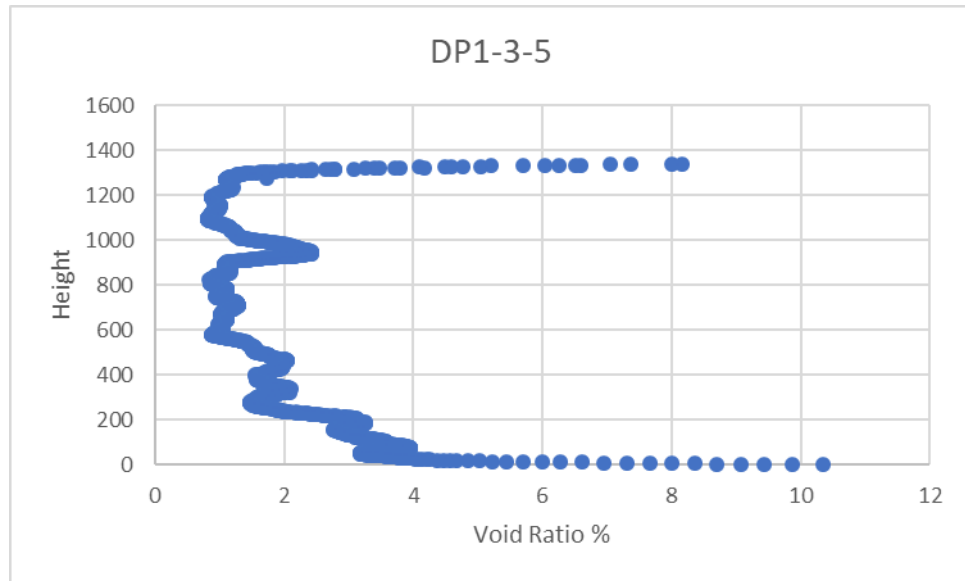
(c)

Figure 20: Graph of void ratio changes in height. (a) DP1-1-5; (b) DP1-2-5; (c) DP1-3-5

A disadvantage of this pixel-level analysis of voids is that it does not provide information about the pore size distribution. A given voids ratio may be due to either many fine pores or a few large ones. Thus, it cannot be used to predict compressive strength since most empirical relationships between strength and porosity require a typical pore size (Mehta and Monteiro, 2006). It would be possible to estimate the pore size distribution from this SNXCT data, but this would require more advanced image analysis software that can operate on 3-D clusters of void pixels to recognize pore shapes.

Chapter 7. Conclusion

This thesis has investigated the application of several image analysis algorithms to SNXCT data sets to quantify the changes in the shape of a concrete object undergoing expansive stresses. DEF damage is conventionally quantified in terms of the one-dimensional linear expansion variable measured by ASTM C157.The assumption has been that it could be applied to a 3-dimensional volume which implies that the expansion is the same in all three directions, i.e., uniform volumetric expansion. However, concrete is not a homogeneous material and the differences in the volume change between the internal aggregates and the cement paste will produce variations in local displacements that are more likely to produce non-uniform expansion. The anticipated outcome of this research would be a set of macroscopic statistics of the DEF process that would more fully and accurately describe the deformations and thus lead to a better understanding of the mechanisms and kinetics involved. The ability to obtain these deformation statistics from the object itself would make the C157 linear measurement redundant and thus eliminate the need to cast a separate set of concrete prisms and to make labor-intensive measurements on them.

For radial expansion, two statistics were investigated: the mean radius and the radial distortion, i.e., the deviation from circularity expressed in terms of Fourier series coefficients. Both of these depend upon the precise identification of the ring of pixels that define the surface of the cylinder. This proved to be difficult because of the

coarse pixel size (25 µm) which led to mixed pixels that produced a gradient rather than a sharp boundary between the interior and exterior points. Consequently, the uncertainty of the mean radius measurement was on the order of the expected radial expansion. This implies that the minimum radial strain that could be detected would be 0.1%. This is the same order of magnitude as the observed linear expansion. However, the variance of the mean radius with height increased by an order of magnitude going from the control specimen to the heat-treated one, which indicates non-uniform volumetric expansion. This also suggests that the variance could be a useful statistic.

The situation was similar for the radial distortion analysis. It was difficult to detect any deviations from circularity (deviatoric strains) given the 25 µm pixel resolution.

For the tilt angle analysis, the center of mass (CM) method of finding the centroid proved to be robust than the method of using extreme horizontal and vertical points because it used all the points in the CT slice. The CM method assumes that the material density is uniform. This approximation was validated for the concrete specimens by the results for the control specimen, which had experienced expansion. The centroids of the successive CT slices showed no detectable deviation from the straight line of the tilt axis. It was found that the data from DP1-3-4 and DP1-3-5 could be pooled providing a total of 3,215 points for the linear regression analysis. This resulted in a very precise estimate of the tilt angle of $2.165 \pm 0.001°$. The fact

that the tilt angle remained constant from one scan to another suggests that it was not due to the swelling of the epoxy during storage in the limewater bath. It was probably introduced during the casting of the specimens or epoxying of the specimen to the base.

A similar analysis could not be carried out for the two heat-treated specimens because the deviations from linearity were too large. These indicate a shear strain caused by non-uniform expansion with height. Their magnitudes are comparable to the variances of the mean radius. The azimuth angle also varied from one slice to another, a sign of twisting.

The template matching algorithm found all the barium titanate microbeads and almost all stainless-steel ones in the X-ray images. However, only 20% of the polystyrene microbeads were detected in DP1.1 during scans 4 & 5 and nearly none in the other two specimens. They were difficult to detect because of low contrast with the cement paste matrix.

The void area ratio ranged from 2.0 – 2.6%. There were no significant trends. However, the segmentation was affected by the variations in the average pixel brightness from one CT slice to another.

The overall conclusions are:

1. The volumetric expansion is not uniform and therefore the linear expansion is not sufficient for characterizing the DEF effect on shape change.

2. The current spatial resolution of the SNXCT system is marginal for measuring expansion.

Appendices

Appendix A: MATLAB code

Code 1: 2-dimensional model using Fourier analysis &

```
function [aj,bj]=f1(j,boundary,centroid)
    R=getR(boundary,centroid);

    ainted(:)=R(:,2).*cos(j.*R(:,1));
    binted(:)=R(:,2).*sin(j.*R(:,1));
aj=trapz(R(1:length(R),1),ainted(:)')/(2*pi);
bj=trapz(R(1:length(R),1),binted(:)')/(2*pi);

function [R,A]=f2(j,boundary,centroid)
count=0;
for jj=0:j
count=count+1;
[aj(count),bj(count)]=f1(jj,boundary,centroid);
end
A=f3(aj,bj);

Ror=getR(boundary,centroid);
R=zeros(length(Ror),2);
    for count=1:length(Ror)
R(count,1)=Ror(count,1);
        for jj=0:j
R(count,2)=aj(jj+1)*cos((jj)*Ror(count,1))+bj(jj+1)*sin((jj)*Ror(count,1))+R(count,2
);
if abs(R(count,2)-Ror(count,2))<0.09
    break;
end
    end
        end

function A=f3(aj,bj)
    %function is acculate the area of the recreate area
    len=length(aj);
    A=pi*aj(1).^2+pi/2*sum(aj(2:len).^2+bj(2:len).^2);

function [R]=getR(boundary,centroid)
```

%function R(θ)={(θ,Rn)} is the length from the center of mass to the

%surface at an angle θ , Rnis the length of these line segments

%getR first coefficients is theta second is length from the mass centroid
%output R is a n*2 matix which is numerically surface
% R=zeros(ceil(length(boundary(:,1))/1),2);
[R(:,1),R(:,2)]=cart2pol(boundary(:,2)-centroid(1),centroid(2)-boundary(:,1));
R(:,1)=pi+R(:,1);
R=sortrows(R,1);

RGB = imread('filename');
figure,imshow(RGB);
bw = imbinarize(RGB);
figure,imshow(bw);
% remove all object containing fewer than 500 pixels
bw = bwareaopen(bw,500);

% fill a gap in the pen's cap
se = strel('disk',2);
bw = imclose(bw,se);
figure,
% fill any holes, so that regionprops can be used to estimate
% the area enclosed by each of the boundaries
bw = imfill(bw,'holes');

imshow(bw);
[B,L] = bwboundaries(bw,'noholes');

% Display the label matrix and draw each boundary
imshow(label2rgb(L, @jet, [.5 .5 .5]))
hold on
for k = 1:length(B)
   boundary = B{k};
   plot(boundary(:,2), boundary(:,1), 'r', 'LineWidth', 2)
end
stats = regionprops(L,'Area','Centroid');

threshold = 0.3;

for k = 1:length(B)

   % obtain (X,Y) boundary coordinates corresponding to label 'k'

```matlab
    boundary = B{k};

    % obtain the area calculation corresponding to label 'k'
    area = stats(k).Area;

        centroid = stats(k).Centroid;
    end
end

title(['Metrics closer to 1 indicate that ',...
        'the object is approximately round']);
  clear aj bj count
count=0;
for j=1:80
count=count+1;
[aj(count),bj(count)]=f1(j,boundary,centroid);
end
figure,plot(1:count,aj,'b-.',1:count,bj,'r-');
xlabel('j');
ylabel('aj(b), bj(r)')
clear A R1 R
for j=0:80
[R1,A(j+1)]=f2(j,boundary,centroid);
R=getR(boundary,centroid);
t=[ceil(R1(:,2).*sin(R1(:,1))+centroid(1)) ceil(R1(:,2).*cos(R1(:,1))+centroid(2))];
figure,
plot(centroid(1)+R1(:,2).*sin(R1(:,1)),centroid(2)+R1(:,2).*cos(R1(:,1)),'r','LineWidth', 3);
end
figure,plot([1:25],A(2:26),'r-',[1:25],area.*ones(1,25));
xlabel('j');
ylabel('Area')
RR=R1 (:,[2]);
   Meanr= mean (RR);
```

Code 2: Create matrix containing the distance from the centroid to the boundary point, 3-dimensional plot of centroid and corresponding polar plot

```matlab
number=dir('File location*.tif'); %Opening a folder in a directory
b=numel(number); %counting the number of files into the folder
for i=1:b
    filename=strcat('File location\',' prefix of File name ',num2str(i+b-1.','%04d'),'.tif');
    GV = imread(filename);
```

```
        bw = imbinarize(GV);
        bw = bwareaopen(bw,500);
        se = strel('disk',2);
        bw = imclose(bw,se);
        bw = imfill(bw,'holes');

        [B,L] = bwboundaries(bw,'noholes');

        stats = regionprops(L,'Area','Centroid');
        [~,index] = sortrows([stats.Area].');
        stats = stats(index(end:-1:1));

        center = stats(1).Centroid;

        r = sqrt((center(1)-centroid1(1))^2+(center(2)-centroid1(2))^2);
        if center(1)> centroid1(1)&& center(2)>centroid1(2)
        phi=atan((center(2)-centroid1(2))/(center(1)-centroid1(1)));

        elseif center(1)< centroid1(1)&& center(2)>centroid1(2)
        phi=pi+atan((center(2)-centroid1(2))/(center(1)-centroid1(1)));

        elseif center(1)< centroid1(1)&& center(2)<centroid1(2)
        phi=pi+atan((center(2)-centroid1(2))/(center(1)-centroid1(1)));

        else center(1)> centroid1(1)&& center(2)<centroid1(2);
        phi=2*pi+atan((center(2)-centroid1(2))/(center(1)-centroid1(1)));
        end
        Allangles(i)=phi;
        Allcenters(i,:)=center;
        A(:,i)=center;
        R(i)=r;
        Zvalue(:,i)=1*i;
end

R=R';
R=flipud(R);

Plotcenter=[ A;Zvalue ];
x=abs(Plotcenter(1,:));
y=abs(Plotcenter(2,:));
z=abs(Plotcenter(3,:));

X=fliplr(x)
```

Y=fliplr(y)

plot3(X,Y,z);
title('Centroid line in 3d space');
xlabel('X');ylabel('Y');zlabel('Z');
xlim([700 1300])
ylim([700 1300])
grid on
Xp=x-centroid1(1);
Yp=y-centroid1(2);

[theta,rho] = cart2pol(Xp,Yp);

Figure (1)
polarscatter(theta, rho,1,'r');
rlim([0 100]);
title ('DP1-2-6 Polar plot of scatter points of centroid point');
grid on

Code 3: Template matching for searching microbeads in images.
Bead=imread('File name of microbead');
number=dir('Location of images*.tif');
b=numel(number);
for k=1: number
     filename=strcat('Location of images\', 'prefix of File name',num2str(k+b-
1.','%04d'),'.tif');
    J=imread(filename);
    C = normxcorr2(Bead,J);
    [ypeak, xpeak] = find(C==max(C(:)));
    max_C= max(C(:));
if max_C> 0.93
     locate=[xpeak,ypeak];
     Height(k,:)=1*k+2;
else
    locate=[0,0];
    Height(k,:)=0;
end
    location(k,:)=locate;

    New=[Height, location];
    New=New(any(New,2),:);

end

New(:,2)= New(:,2)-22; % 22 is the half size of template
New(:,3)= New(:,3)-22; % New is the matrix of combination of height and location

Code 4: Find the void ratio through image analysis

```
number=dir('File location*.tif');
b=numel(number);
for k=1:b
    filename=strcat('File location\',' prefix of File name ',num2str(k+b-1.','%04d'),'.tif');
    GV = imread(filename);
    bw = imbinarize(GV);
    % remove all object containing fewer than 30 pixels
    bw = bwareaopen(bw,500);

% fill a gap in the pen's cap
    se = strel('disk',2);
    bw = imclose(bw,se);

% fill any holes, so that regionprops can be used to estimate
% the area enclosed by each of the boundaries
    bw = imfill(bw,'holes');

    imagenew = bw.*GV;

    imagenew(imagenew == 0)= NaN;

    [counts,centers] = hist(imagenew,1024);

    [N,edges] = histcounts(imagenew,1024);
    CC=centers';
    L=[CC;N];
    List=L';
for i = 1: length(List)
    if List(i, 1) < 0.9
        newlist1(i, 1) = List(i, 1);
        newlist1(i, 2) = List(i, 2);
    else
        newlist1(i, 2) = 0;
    end
end
A=sum(newlist1 ,1);
B=sum(List ,1);
```

```
Voidcount=A(:,2);
Slicecount=B(:,2);
VR=Voidcount/Slicecount;
Voidratio(k)=VR;
end
Totalratio=sum(Voidratio)/k;
```

* These are the raw data of height and the actual height needs further processing.

Serial Number	DP1-1-4	DP1-1-5	DP1-1-6
Location & Height	(1725,556) 435	(1814,1118) 388	(237,1339) 405
	(268,528)473	(848,1821) 490	(1327,1464) 499
	(592,190) 545	(870,1726) 529	(882,475) 530
	(1394,668) 565	(1464,1121) 534	(519,1182) 537
	(853,1336) 569	(742 643) 546	(1266,1396)544
	(652,274) 578	(886,1702) 584	(1243,1387) 555
	(670,292) 598	(732,574) 588	(856,416) 583
	(866,1405) 625	(694,1279) 600	(1206,962) 594
	(615,749) 638	(385,705) 627	(1193,363) 617
	(481,1227) 1214	(420,859) 1203	(440,431) 766
	(1527,262)1235	(778,829) 1276	(1238,504) 1129
	(828,1149) 1310	(776,829) 1282	(939,639) 1214
	(1079,1134) 1313	(1021,768) 1290	(714,701) 1225
	(919,1770) 1551	(1720,922) 1520	

Serial Number	DP1-2-4	DP1-2-5	DP1-2-6
Location (coordinates) & Height	(1703,661) 457	(327,1453) 452	(558,174) 503
	(268,528) 473	(1102,1005) 510	(838,973) 563
	(991,1053)	(877,911)	(948,772)

	542	599	640
	(984,810) 634	(957,377) 632	(1398 949) 680
	(1491, 683) 677	(729,440) 671	(1386,724) 693
	(1326,482) 690	(957,960) 1043	(891,837) 1050
	(972,903) 1073	(1210,930) 1128	(873,1073) 1126
	(1101,1121) 1150	(970,787) 1143	(845,1063) 1135
	(1133 845) 1170	(1191,943) 1146	(1045,880) 1143
	(1423,1396) 1221	(600,188) 1170	(1018,353) 1176
	(1426,1392) 1247	(414,924) 1175	(1640,635) 1178
	(166,752) 1279	(1592,748) 1194	(971,1449) 1197
	(1527,262) 1235	(1592,744) 1220	

Serial Number	DP1-3-4	DP1-3-5	DP1-3-6
Location (coordinates) & Height	(1751,737) 219	(321,1418) 238	(489,176) 204
	(1132,762) 376	(908,1218) 384	(320,443) 229
	(839,794) 520	(1280,1708) 417	(1289,278) 282
	(772,1596) 587	(1180.1105) 526	(646,726) 350
	(1677,875) 634	(1018,313) 588	(739,981) 482
	(643,992) 646	(1313,859) 650	(1471,867) 542
	(71,802) 672	(1917,879) 673	(959,1114) 597
	(613,681) 677	(1429,1150) 681	(686,1208) 627
	(819,363) 691	(1321,1515) 687	(356,1092) 640

(1445,820) 1061	(591,1253) 1076	(630,434) 982
(1192,1084) 1127	(758,924) 1130	(922,602) 1040
(696,506) 1207	(1396,1344) 1215	(512,1172) 1117
(1031,869) 1286	(1149,1173) 1337	(765,793) 1189
(886,738) 1325	(678,951) 1220	(678,952) 1223
(874,1160) 1361		
(833,997) 1382		

Bibliography

Cartz, L. (1995). Nondestructive testing: Radiography, ultrasonics, liquid penetrant, magnetic particle, eddy current. *Materials Park, OH: ASM International*. (pp. 15-19)

Ceesay, J. (2007). *Characterization of damage in mortar and concrete specimens due to delayed ettringite formation (def)* (Doctoral dissertation, University of Maryland, College Park, 2007). University of Maryland.

Erdogan, S. T., Quiroga, P. N., Fowler, D. W., Saleh, H. A., Livingston, R. A., Garboczi, E. J., ... & Satterfield, S. G. (2006). Three-dimensional shape analysis of coarse aggregates: New techniques for and preliminary results on several different coarse aggregates and reference rocks. *Cement and Concrete Research*, *36*(9), 1619-1627.

Feuze Lekem, S. A. (2019) *Investigation of Delayed Ettringite Formation Damage Process Using Simultaneous Neutron and X-ray Tomography* (Doctoral dissertation, University of Maryland, College Park, 2019). University of Maryland.

Fu, Y., & Beaudoin, J. J. (1996). Microcracking as a precursor to delayed ettringite formation in cement systems. *Cement and concrete research, 26*(10), 1493-1498.

Garboczi, E. J. (2002). Three-dimensional mathematical analysis of particle shape using X-ray tomography and spherical harmonics: Application to aggregates used in concrete. *Cement and concrete research*, *32*(10), 1621-1638.

Ghorab, H. Y., Heinz, D., Ludwig, U., Meskendal, T., Wolter, A. (1980). "On the Stability of Calcium Aluminates Sulphate Hydrates in Pure Systems in Cements," *7th Intnl. Congr. Chem. Cem.*, *Vol. IV,* 496-503.

Kennerley, R. A. (1965, May). Ettringite formation in dam gallery. In *Journal Proceedings* (Vol. 62, No. 5, pp. 559-576).

Lucero, C. L., Bentz, D. P., Hussey, D. S., Jacobson, D. L., & Weiss, W. J. (2015). Using neutron radiography to quantify water transport and the degree of saturation in entrained air cement based mortar. *Physics Procedia*, *69*, 542-550.

Sangwin, C. J. (2006). Locating the center of mass by mechanical means. *Journal of the Oughtred Society*, *15*(2), 16-18.

Scherer, G. (1999). Crystallization in pores. *Cement and Concrete Research, 29*(8),

1347-1358.

Shapiro, V. (1993, September). Cross-correlation with reconstruction: A new approach to pattern matching. *In International Conference on Computer Analysis of Images and Patterns* (pp. 548-555). Springer, Berlin, Heidelberg.

Taylor, H., Famy, C., & Scrivener, K. (2001). Delayed ettringite formation. *Cement and Concrete Research, 31*(5), 683-693.

Yang, R., Lawrence, C. D., Lynsdale, C. J., & Sharp, J. H. (1999). Delayed ettringite formation in heat-cured Portland cement mortars. *Cement and Concrete Research*, *29*(1), 17-25.

Yoo, J. C., & Han, T. H. (2009). Fast normalized cross-correlation. *Circuits, systems and signal processing*, *28*(6), 819.

Zeissler, C. J., & Lindstrom, A. P. (2010). Spectral measurements of imaging plate backgrounds, alpha-particles and beta-particles. *Nuclear Instruments and Methods in Physics Research Section A: Accelerators, Spectrometers, Detectors and Associated Equipment*, *624*(1), 92-100.